4. CURRENT DRIVE

Tak-Kuen Mau David A. Ehst John Mandrekas

Contents

4. CURRENT DRIVE

4.1. INTRODUCTION

The ARIES-I design is a conceptual commercial reactor based on modest extrapolation from the present tokamak physics data base. For a commercial reactor, steady-state operation is preferable because of the many undesirable features of pulsed operation (such as thermal fatigue of in-vessel components and magnets and the requirement for a thermal-energy storage system), which lead to a short reactor lifetime and high costs. For an economical steady-state reactor, the recirculating power fraction should be <20%. This can be achieved by reducing the amount of plasma current to be driven by external means (*i.e.*, minimizing the total plasma current and maximizing the bootstrap-current fraction) and also by using an efficient, cost-effective current-drive technique.

The ARIES-I design operates at a relatively high plasma aspect ratio ($A = 4.5$), a low plasma current ($I_p = 10.2$ MA), and a high on-axis magnetic field ($B_o = 11.3$ T). As a result, the poloidal beta is high and a high bootstrap-current fraction of 0.68 is predicted. Because of the low plasma current and high bootstrap-current fraction, only 3.3 MA of current should be driven by external means. Therefore, a steady-state reactor with relatively small current-drive power is possible. The key parameters of the ARIES-I reactor are listed in Table 4.1-I. For the ARIES-I reactor, fast magnetosonic waves in the ion-cyclotron range of frequencies are selected as the primary technique for current drive. The high magnetic field also provides a unique environment for considering fast-wave current drive (FWCD) in a frequency range where the attractive features of a folded-waveguide antenna can be exploited. The high-density scrape-off layer ($n_s = 0.87 \times 10^{20}$ m^{-3}), as required by high-recycling divertors, may facilitate the coupling of wave power to the plasma. From safety and environmental considerations, silicon-carbide fiber composites are proposed as the structural material for the ARIES-I blanket. For similar reasons, this material may be considered in the waveguide launching structures.

Here, various physics aspects of the ARIES-I current-drive system are described. Section 4.2 describes the selection process, based on the general design philosophy, for a suitable current driver. Section 4.3 is devoted to the detailed calculation of the bootstrap current in the ARIES-I reference equilibrium. In Sec. 4.4, the physics of FWCD is described, including the experimental data base, theoretical efficiency, and determination of the required wave spectrum and launching location via ray-tracing analysis. Section 4.5

contains a detailed account of the design features of the folded-waveguide antenna and its predicted performance in ARIES-I in terms of coupling efficiency and directivity. This is followed by a report on the projected performance of the overall FWCD system, including the source. Neutral-beam current drive is considered as an attractive alternative to fast waves and, therefore, it is also studied in considerable detail for ARIES-I (Sec. 4.6). A summary of the ARIES-I current-drive system and critical issues are given in Sec. 4.7.

Table 4.1-I.
Key Parameters of the ARIES-I Reactor

Major radius, R (m)	6.75
Minor radius, a (m)	1.50
Aspect ratio, A	4.50
Elongation, κ	1.80
Triangularity, δ	0.70
Magnetic field at coil, B_c (T)	21.00
Magnetic field on axis, B_o (T)	11.33
Plasma current, I_p (MA)	10.20
Safety factor on axis, q_o	1.30
Edge safety factor, q_*	3.90
Peak electron density, n_{e0} (10^{20} m^{-3})	1.88
Average electron density, n_e (10^{20} m^{-3})	1.45
Separatrix electron density, n_s (10^{20} m^{-3})	0.87
Peak electron temperature, T_{e0} (keV)	36.62
Average (density-weighted) electron temperature, T_e (keV)	19.3
Volume-averaged electron temperature, $\bar{T}_e$ (keV)	17.44
Toroidal beta, β_t (%)	1.90
Effective charge, Z_{eff}	1.65
Bootstrap-current fraction, I_{BS}/I_p	0.68

4.2. CURRENT-DRIVER SELECTION

Even though the design value of the plasma current in ARIES-I is relatively small (because of the high bootstrap-current fraction), a crucial parameter affecting the cost of electricity (COE) of the reactor is the efficiency of the current-drive system, measured by the figure of merit, $\gamma \equiv n_e I_p R / P_{CD}$. Equally important is the wall-plug to first-wall efficiency of the power delivery system associated with the current-drive technique. Furthermore, the system unit cost ($/W), which depends on the method of power generation and transport and on the maturity of the technology involved within the time frame of application, is an important consideration.

At the same time, there are other important but less quantifiable factors that affect the desirability of a current-drive technique: (1) ensuring the compatibility of the current-drive-system components with the high neutron-flux and radiation environment; (2) addressing or avoiding neutron irradiation, activation, and tritium buildup in the subsystems located in front of the shield; (3) minimizing intrusion into the first wall, blanket, and shield by the current-drive-system components in order to minimize the impact on tritium breeding and normal maintenance procedures; (4) designing for flexibility and versatility so that the system can perform multiple functions other than current drive (*e.g.*, plasma initiation, current ramp-up, auxiliary heating-to-ignition conditions, central plasma fueling, and current profile tailoring for MHD stability and disruption control).

4.2.1. Steady-State and Pulsed Operations

There is a clear desire to operate tokamak reactors in a pure steady-state mode, if the capital cost and recirculating electric power of the current-drive system are not too large. These issues were explored in Refs. [1, 2], where various pulsed and quasi-steady-state burn cycles were compared with steady-state operation. In this section, results of this comparison study are summarized and the advantages of steady-state operation over pulsed operation are elucidated in a quantitative fashion.

A maximum burn period, t_f, is desirable to minimize damage to plasma-facing components from thermal fatigue, temperature limits, sputtering, and disruption erosion. Even with infrequent disruptions (once per thousand cycles), long burn times ($t_f \geq 3000$ s) are needed so disruption damage does not breach the first wall/limiter or divertor plates before the radiation life limit occurs (5–10 operating years, depending on the structural material). An ohmic transformer suffers mechanical fatigue with pulsed operation, necessitating substantial cost increases to add structural support (reducing cyclic stress) when

the number of pulses, N, exceeds $\sim 10^4$. Likewise, out-of-plane bending of the toroidal-field (TF) coils, due to the overturning torques caused by the equilibrium-field (EF) coils, will necessitate expensive structural additions if $t_f \leq 7000$ s. Such burn goals can barely be met with an ohmically driven reactor the size of ARIES-I, even assuming plasma conductivity is the Spitzer value (*i.e.,* without neoclassical reductions). Figure 4.2-1 shows that $t_f \leq 3000$ s and $N \geq 10^5$ are more realistic expectations for a pulsed reactor.

Additional expenses associated with pulsed operation are electric power supplies required for rapid ramp-down and ramp-up between burn pulses and also for thermal energy storage during the dwell, as required to keep the turbine generator operating under constant power. The study showed that the sum of these two costs is minimized for dwell periods of $\sim$15–40 s. Even with advanced thermal-storage technology (liquid metals), the costs of these combined systems is approximately \$400 M for pulsed reactors, which should be compared to an estimated \$10 M for steady-state operation (assuming long, several-minute current-ramp times during start-up). These capital cost penalties associated with pulsed operation are summarized in Fig. 4.2-1. The upper curves show that, relative to the cost of the STARFIRE reactor [3] which operated at steady state, the cost must be $\sim$25%–40% more for a pulsed tokamak to provide the same performance.

The STARFIRE design, however, incorporated a very efficient current-drive system which had a negligible impact on circulating power and capital cost. Thus, it is important to quantify the required current-drive performance needed to achieve an economic advantage with steady-state operation. This information is presented in Fig. 4.2-2 for different capital costs of delivered current-drive power to the plasma and for different electrical efficiencies, η_d, of the current-drive system. Taking \$1.25/W to be typical of fast-wave current drive (FWCD) systems, one finds that the normalized current-drive efficiency in the plasma must be $\gamma \geq 0.3$ in order to have a smaller capital cost than a pulsed reactor; whereas $\gamma \geq 0.5$ is needed to achieve large net power ($P_{net} \geq 1200$ MW), provided a reasonable electrical efficiency ($\eta_d \geq 0.5$) is possible. Analyses of the ARIES-I design show that $\gamma^B \simeq 1.0$ can indeed be achieved with the aid of the bootstrap effect. Therefore, it is clearly preferable to elect steady-state operation for the present design.

4.2.2. Survey of Current-Drive Options

Based on theoretical analyses and, in some cases, experimental data on conventional current-drive techniques such as neutral beams and electromagnetic waves [4], the projected γ for reactors falls in the range of 0.3–0.6. For this range of γ, systems code calculations indicate that the cost of driving currents can significantly impact the cost of

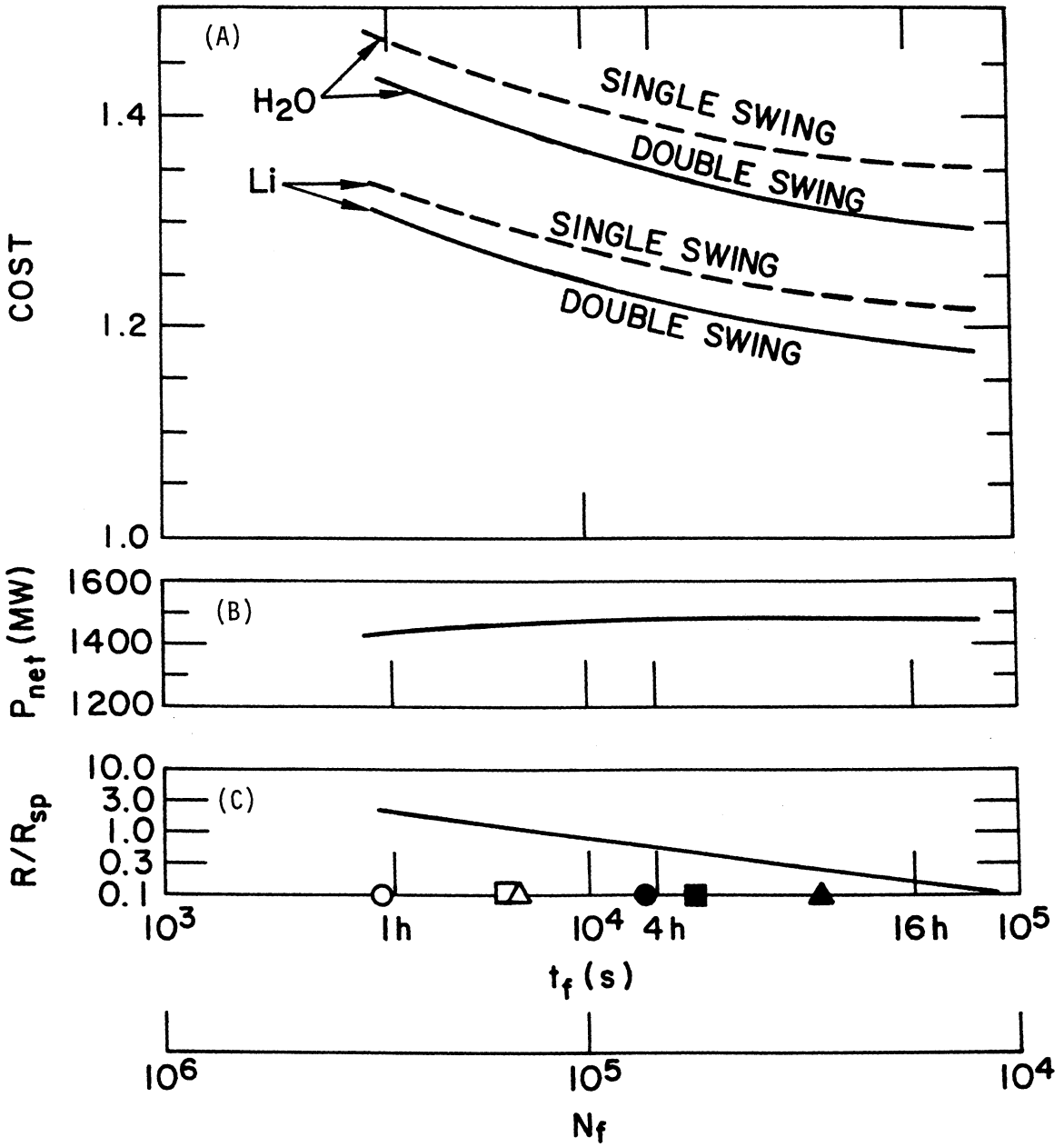

Figure 4.2-1. Ohmic burn cycle for $B_{OH} = 10$ T, 8-m reactor: (A) The total direct capital cost normalized to STARFIRE [3] (upper curves are water thermal storage and near-term magnet costs, C_I, and lower are liquid-sodium thermal storage and long-term magnet costs, C_{II}); (B) Net electric power; and (C) Plasma resistance required to obtain t_f, normalized to Spitzer resistivity, R_{sp}, with $Z_{eff} = 1.70$, $\bar{T}_e = 10$ keV, and $I_o = 13.0$ MA. Solid symbols are burn goals for worst case disruptions and thermal fatigue, while open symbols are goals for moderate disruption damage (open circle is for limiter's leading edge, square is for limiter's front face, and triangle is for the first wall).

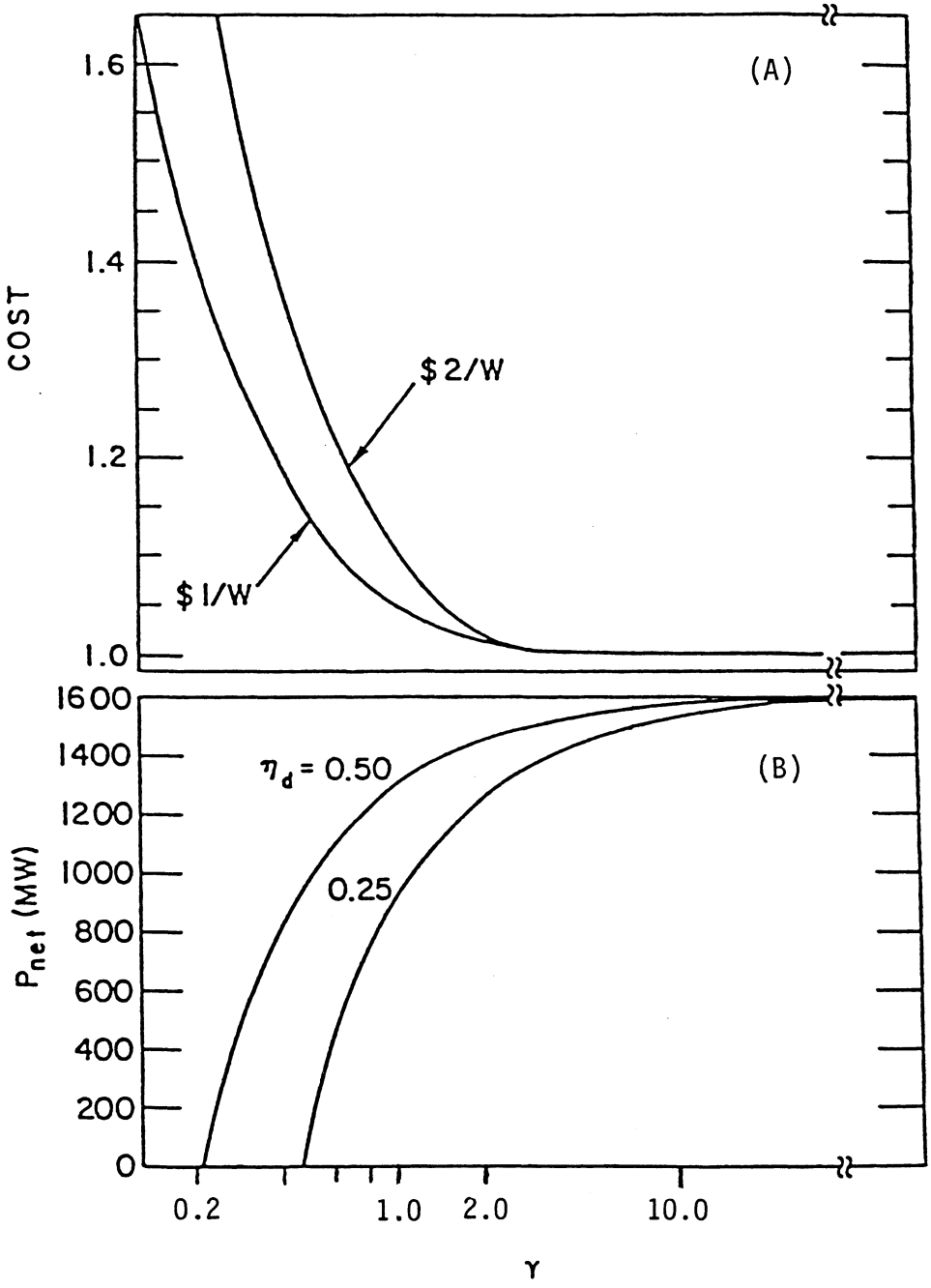

Figure 4.2-2. Steady-state burn cycle for a 7-m major radius reactor with $\bar{T}_e = 12$ keV, $n_{20} = 1.9$, and $I_o = 14.8$ MA: (A) Direct capital cost for two values of current-drive-system cost (EF-coil winding costed with C_{II} formula) and (B) Net electric power.

electricity of the reactor. Thus in optimizing the current-drive scenario, it is imperative that the amount of externally driven current be reduced as much as possible. Fortunately, in the tokamak geometry, a self-induced bootstrap current exists in the plasma as a result of diamagnetic and neoclassical drift-orbit effects in the collisionless regime [5]. The bootstrap current has been indirectly observed in many large tokamak experiments such as TFTR [6], JET [7], and JT-60 [8]. The recent result from JT-60 is particularly impressive. A bootstrap-current fraction as high as 80% was inferred from experimental data in a high poloidal-beta discharge ($\beta_p = 3.2$) with 20 MW of neutral-beam injection power. Indeed, the ARIES-I reactor operates with a relatively high A, low I_p, and high β_p in order to maximize the bootstrap-current fraction (Sec. 4.3).

To identify attractive, potential candidates for external current drive in ARIES-I, a large number of current-drive techniques have been surveyed. In general, they can be classified into two categories according to the energy range of the particles carrying the current: energetic and bulk (or thermal) carriers. In energetic-carrier current drive, the externally applied power interacts resonantly with the plasma to create a super-thermal non-Maxwellian population in the particle velocity distribution that, when balanced against the background plasma in momentum space, creates a net current flowing in the toroidal direction. Conventional current-drive techniques, such as neutral beams and waves, fall into this category. Because energy is required to maintain the energetic population against collisional thermalization, the current-drive power scales approximately as n_e/T_e. This implies that energetic-carrier current drive is most efficient in low n_e and high T_e plasmas (conditions that conflict with those required for effective fusion ash exhaust and for high-recycling poloidal divertors).

On the other hand, bulk-carrier current-drive mechanisms impart net momentum uniformly to the entire particle population. Examples of this category of current-drive technique include ohmic inductive drive, helicity injection (including ac [9] and dc [10]), and compact-torus injection [11]. The latter two techniques rely on transferring helicity, or poloidal flux in a tokamak configuration, through relaxation processes [12]. A recent addition to the bulk carrier category is the radio-frequency (RF) helicity-injection technique [13] in which a low frequency wave ($f \sim \Omega_i$), with helicity content in the form of a dominant circular polarization, is coupled into and strongly damped in the plasma via cyclotron resonance processes, thereby transferring poloidal flux locally to the plasma. The attractive feature of these techniques is that power is dissipated ohmically in the plasma and at the edge. This power then scales as $T_e^{-3/2}$, is not n_e-dependent, and results in much higher current-drive efficiency than that of energetic carrier drivers. The technological requirements for these current-drive systems appear to be modest.

The ARIES-I design guidelines call for a conservative approach with respect to extrapolation from the present tokamak physics data base. The choice of the current-drive technique, therefore, should be based on sound physics understanding and on experimental data in order to project with confidence its performance into the reactor regime. The basic physics of energetic-carrier current drive is generally well understood because of a decade of extensive studies [4]. Successful demonstration experiments have also been performed, where a fraction or even all of the plasma current was sustained by either lower-hybrid waves [14, 15], neutral beams [16], or fast waves [17]. On the other hand, experimental studies of helicity-injection current drive are presently in the preliminary stages [18, 19]; dc helicity injection, in particular, has met with some success (up to 3.5 kA of current driven in CCT) [20]. Nevertheless, the present theoretical understanding of these current-drive mechanisms is too weak to permit extrapolation to reactor parameters with confidence. The key issues appear to be the identification of the relaxation process that is responsible for the penetration of the injected helicity, and the effect of this process on global plasma properties (*e.g.*, equilibrium, stability, and confinement). Therefore, based on the ARIES-I design guidelines, bulk-carrier current drivers are excluded from further consideration, even though their projected efficiency exceeds that of more conventional drivers.

4.2.3. Current-Drive Techniques for ARIES-I

For ARIES-I, the conventional energetic-carrier current-drive techniques that have been considered include electron-cyclotron waves, lower-hybrid waves, neutral beams, and fast waves in the higher-harmonic, ion-cyclotron, and low-frequency ($f < \Omega_i$) regimes. More advanced variations of the energetic carrier techniques (including beat waves, rising buckets, and stochastic acceleration in the electron-cyclotron range of frequencies) [21] and high-power pulsed lower-hybrid waves [22] have not been considered because of insufficient physics understanding, no experimental data base, and modest efficiency or excessive unit cost. The conventional electron-cyclotron current drive is considered undesirable for ARIES-I because of its low efficiency ($\gamma \leq 0.25$) and its high unit cost ($4/W), even though it has the capability of detailed local current-profile control and is, therefore, an ideal technique for disruption control.

A large number of lower-hybrid current-drive experiments have been performed on tokamaks, often with impressive results [4]. To date, the most notable results come from JT-60 [23], where a record γ of 0.34 was measured. Current initiation, ramp-up, and steady-state current drive have all been demonstrated [24], and soft X-ray measurements

appear to indicate that the driven current is peaked on the magnetic axis; but, as the plasma temperature increases, the window of wave refractive indices for core penetration will diminish. Thus in reactor plasmas with $T_{e0} \gg 20$ keV, lower-hybrid waves will not have access to the center of the plasma where a seed current needs to be maintained. Because of its rather high efficiency, lower-hybrid current drive will be used to ramp up the current in the start-up phase and to drive current in the plasma periphery during steady-state operation.

Although the interaction of fast waves in the higher harmonic regime with electrons has been demonstrated in present-day tokamaks [17], applicability to reactors as the current driver is substantially diminished by the dominant absorption of its power by energetic α-particles [25]. Low-frequency FWCD, on the other hand, relies on the weak multiple-pass absorption of the wave power by high energy electrons ($v_{||} \gg v_{te}$) and, therefore, has a high efficiency ($\gamma > 0.4$). In fact, it may even be desirable to excite moderate-Q toroidal eigenmodes in order to increase the coupling to the plasma. There are, however, many unresolved issues related to this current-drive technique: the effect of the presence of Alfvén resonance inside the plasma on the wave deposition profile, the competing wave-absorption processes near the plasma edge, and the potential loss of wave spectrum control as a result of wave-number scattering by density fluctuations in the plasma periphery. In addition, the scarcity of experimental data in large tokamaks and the need to use large launching structures in this frequency range eliminate this technique from consideration for ARIES-I.

The two remaining options, neutral-beam current drive (NBCD) and ion-cyclotron range-of-frequencies (ICRF) fast-wave current drive (FWCD), can both be used for ARIES-I. Various aspects of these two current-drive techniques have been investigated with respect to their applicability to reactors. A comparison of these issues is given in Table 4.2-I. The three parameters that directly impact the reactor economics are γ, system efficiency (ratio of current-drive power to the electric power delivered to the source, η), and system unit cost. Multi-MeV NBCD systems have a higher efficiency ($\gamma \sim 0.5$–0.6) and high unit costs (\$3/W) relative to FWCD efficiency ($\gamma \sim 0.3$–0.4) and unit costs (\$1/W). As a result, the capital cost of the FWCD system is smaller, especially if the cost of NBCD building is taken into account, but requires slightly higher recirculating power. The FWCD uses conventional, "off-the-shelf" technology that requires only a modest developmental effort to reach the desired performance level for ARIES-I. The NBCD, on the other hand, requires an extensive research program to develop practically every component in the system and, therefore, the projected system efficiency is less certain.

Table 4.2-I.
A Comparison of Fast-Wave and Neutral-Beam Current-Drive Systems

	Neutral Beam	Fast Wave
Current-drive efficiency	$\gamma \sim 0.5$–0.6 ($E_b > 2$ MeV)	$\gamma \sim 0.3$–0.4 (improvement possible)
System efficiency	$\eta \sim 0.68$ (RFQ) $\eta \sim 0.75$ (ESQ)	$\eta \sim 0.70$ (100–200 MHz)
Unit cost	\$3/W (RFQ & ESQ)	\$1/W (100-200 MHz)
Physics understanding	Very good (simple)	Very good (complicated)
Experimental data base	Good	Fair
Current drive	(DITE, DIII-D, JT-60, TFTR)	(JIPPTII-U, JFT-2M, planned on DIII-D, JET)
Other	(H-mode, bootstrap, enhanced L-mode)	(H-mode, direct e-heating on JET, JT-60, JFT-2M)
Auxiliary heating	Good (shine-through)	Very good (need tunable RF source)
Current ramp-up	Fair (shine-through)	Fair (multiple-pass absorption)
Current profile control	Good (column of beamlets, tangency radii)	Good (off mid-plane launch, spectrum control)
Core penetration	Good (need high E_b)	Very good (natural focusing)
Impurities	Not an issue	Minimized by Be coating, spectrum peak, SiC wall
Technology extrapolation	Substantial (negative ion source, superconducting RFQ, laser neutralizer, RF power supply)	Modest (RF power supply, RF launchers, phase-shift circuits)
Reactor compatibility	Fair (tritium permeation, neutron backstreaming, long beamlines, bulky components)	Good (in-blanket launchers, flexible transmission system, good shielding for major components)
Maintainability	Fair	Good
First-wall intrusion	Acceptable (high-E_b RFQs)	Acceptable (folded waveguides)

At present, neutral beams have accumulated a current-drive data base that is superior to fast waves. However, it should be noted that direct electron heating via the transit-time magnetic-pumping process of the fast waves has been verified in several major experiments (*e.g.*, JET, JT-60, and JFT-2M) and a definitive FWCD experiment in DIII-D is planned for the near future. From the viewpoint of compatibility with the fusion power core, NBCD systems are perceived to be undesirable for reactor application because the component complexity and large size negatively impact the maintainability, availability, and compactness of the reactor plant. In contrast, an equivalent FWCD system does not face these issues because of its flexible and more compact components. Based on the above considerations, FWCD is chosen as the reference current-drive technique for ARIES-I and, as such, is the focus of most of the design work (Secs. 4.4 and 4.5). The NBCD system is also studied as a viable alternative (Sec. 4.6).

4.3. BOOTSTRAP CURRENT

The presence of the bootstrap current, as verified recently in a series of large tokamak experiments [6–8], offers the prospect of reducing the amount of externally driven current. This possibility becomes particularly important if only moderately efficient current drivers are available, as is the case for ARIES-I (Sec. 4.2.3). As a result, maximizing the bootstrap-current fraction, $f_{BS} \equiv I_{BS}/I_p$, is one of the primary tasks in designing a viable current-drive scenario for the reactor. For a fixed aspect ratio, increasing the plasma poloidal beta, or lowering the equilibrium plasma current, is found to be most effective in raising f_{BS}. In the case of ARIES-I, this technique also involves raising the safety factor on axis, q_o, substantially above unity. Based on the most recent experimental data and theoretical predictions, a bootstrap fraction of $\sim$0.7 appears attainable in the ARIES-I configuration. In this section, the neoclassical theory and calculational model of the bootstrap effect are described briefly. This model is incorporated into an equilibrium code coupled to a fast-wave ray-tracing package and used to calculate the amount of the bootstrap current of the reference ARIES-I equilibrium.

4.3.1. Theory and Experimental Data Base

In straight magnetic fields, because of the finite extent of the Larmor radii, perpendicular diamagnetic currents flow in plasmas with density or temperature gradients even though the guiding centers of the particles are stationary. An analogous situation occurs in toroidal systems in which a "bootstrap" current [5] flows parallel to the

magnetic field because of the finite banana width of trapped-particle drift orbits. This effect maximizes in the low-collisionality banana regime in which the banana centers are stationary. At large aspect ratio, A, this neoclassical effect was calculated for all collisionality regimes and for various ion charge states, Z. A comprehensive summary of the derivation is reviewed in Ref. [26], in which the important flux-surface-averaged quantity, $H(\psi) = \langle j_{\|}^{B} B \rangle \, / \, \langle B^2 \rangle$, is derived. Here $j_{\|}^{B}$ is the parallel bootstrap-current density, B is the field amplitude, and $\langle \cdot \rangle$ denotes a flux surface average. The quantity $H(\psi)$ is a function of the poloidal flux surface and of the several variables characterizing each flux surface: local inverse aspect ratio, $\epsilon = A^{-1}$, effective charge, Z, temperatures, T_e and T_i, densities, n_e and n_i, and the various temperature and density gradients. The quantity $H(\psi)$ is roughly proportional to the gradients, and the coefficients vary with temperatures and densities as the collisionality regime changes. Collisionality is measured by the effective collision frequencies ν_{*e} and ν_{*i} (for electrons and ions, respectively). When $\nu_* \ll 1$, a species is well into the banana regime, whereas $\nu_* \geq 1$ implies the plateau regime (which occurs near the magnetic axis and at the cold edge).

The inclusion of bootstrap and RF current drive into a self-consistent calculation of the axisymmetric tokamak equilibrium was formulated in Ref. [27], and an extensive survey of the RF power savings for steady-state operation, due to the aid of the bootstrap effect, was provided in Ref. [28]. In the latter reference, the fractional power reduction was found to be

$$\Gamma \equiv 1 - \frac{\gamma}{\gamma^B} = 1 - \frac{P_{RF}^B}{P_{RF}} = 0.26\, C^{\star}\, A^{-1/2}\, \beta_{Io}\,, \qquad (4.3\text{-}1)$$

where $C^{\star}$ is a function of the plasma parameters and gradients and β_{Io} is the peak Shafranov poloidal beta. In the case where $I_{BS} \ll I_p$, $f_{BS} \simeq \Gamma$ is a good approximation. Without bootstrap currents, the RF power, P_{RF}, may be very large for steady-state current drive; in the presence of the bootstrap effect however, the RF power, P_{RF}^B, may be much smaller, so Γ can approach unity. The first tokamak to reside in the banana regime, the beam-heated ISX-B, provided an early test of the bootstrap theory. Analysis called to question whether the predicted effect was correct [29], although the plasma profile diagnostics on ISX-B may have been inadequate to accurately measure the plasma parameters. In a well-diagnosed toroidal octopole experiment, however, both the bootstrap and Pfirsch-Schlüter currents were clearly measured [30]. Soon high-power heating on several tokamaks provided resounding evidence of the bootstrap current (*e.g.*, TFTR [6], JET [7], DIII-D [16], ASDEX [31], and JT-60 [8]).

4.3.2. Calculational Model

During the ARIES-I study an improved theory of the bootstrap effect, which more accurately treats finite aspect ratio, was provided by Hirshman [32], and this was incorporated into the self-consistent current drive and MHD equilibrium solution with the RIP code [28]. As will be shown, this more accurate formulation by Hirshman can produce significantly different $H(\psi)$ values than the Hinton and Hazeltine results [26]. As noted earlier, $H(\psi)$ is a function of many variables (*e.g.*, Z, ϵ, ν_{*e}, ν_{*i}, and the temperature and density profiles) so it is difficult to directly compare theoretical results. For this study, it was chosen to compute $H(\psi)$ for typical ARIES-I reactors with both the old and new theories. Figure 4.3-1 compares normalized $H(\psi)$ values at three different flux surfaces for a peaked density and flat temperature profile. At finite ϵ (≥ 0.1) in the banana regime [Fig. 4.3-1(B) and (C)], the Hinton and Hazeltine value significantly overestimates the correct Hirshman value.

In contrast, when the density profile is flat and the temperature profile is peaked (more typical of ARIES-I), the Hinton and Hazeltine result is much smaller than that predicted by Hirshman's theory, as shown in Fig. 4.3-2. Focusing on Fig. 4.3-2(B), it is seen that at finite ϵ and deep into the banana regime, the Hinton and Hazeltine result is about half of the Hirshman value. The non-monotonic dependence of the Hinton and Hazeltine result on ν_* is incorrect, and this limitation at $\nu_* \leq 10^{-2}$ was pointed out in the original work [26].

The problem now is how to utilize the Hirshman formulas, which are accurate at all ϵ but only for $\nu_* \leq 10^{-2}$, in the higher collisionality regimes. This is accomplished in the RIP code by using a logarithmic interpolation between the Hirshman and the Hinton and Hazeltine formulas in the region $0.1 \leq \nu_* \leq 1.0$. Since most of the ARIES-I plasma has $\nu_* \leq 0.1$, the Hirshman result basically determines the expected bootstrap-current density. The chain-dashed curves in Fig. 4.3-3 show $H(\psi)$ from the Hinton and Hazeltine theory and from the revised Hirshman formulation for ARIES-I. The new formula yields about 20% larger values, and the bootstrap-current density is seen to be a large fraction of the total current density of the stable ARIES-I equilibrium.

4.3.3. Predicted Bootstrap Current for ARIES-I

Guidance in selecting plasma profiles was found by examining BALDUR transport-code runs (Sec. 3.3). Several profiles are possible, depending on how the transport coefficients are chosen. In general, density profiles are expected to be rather flat since

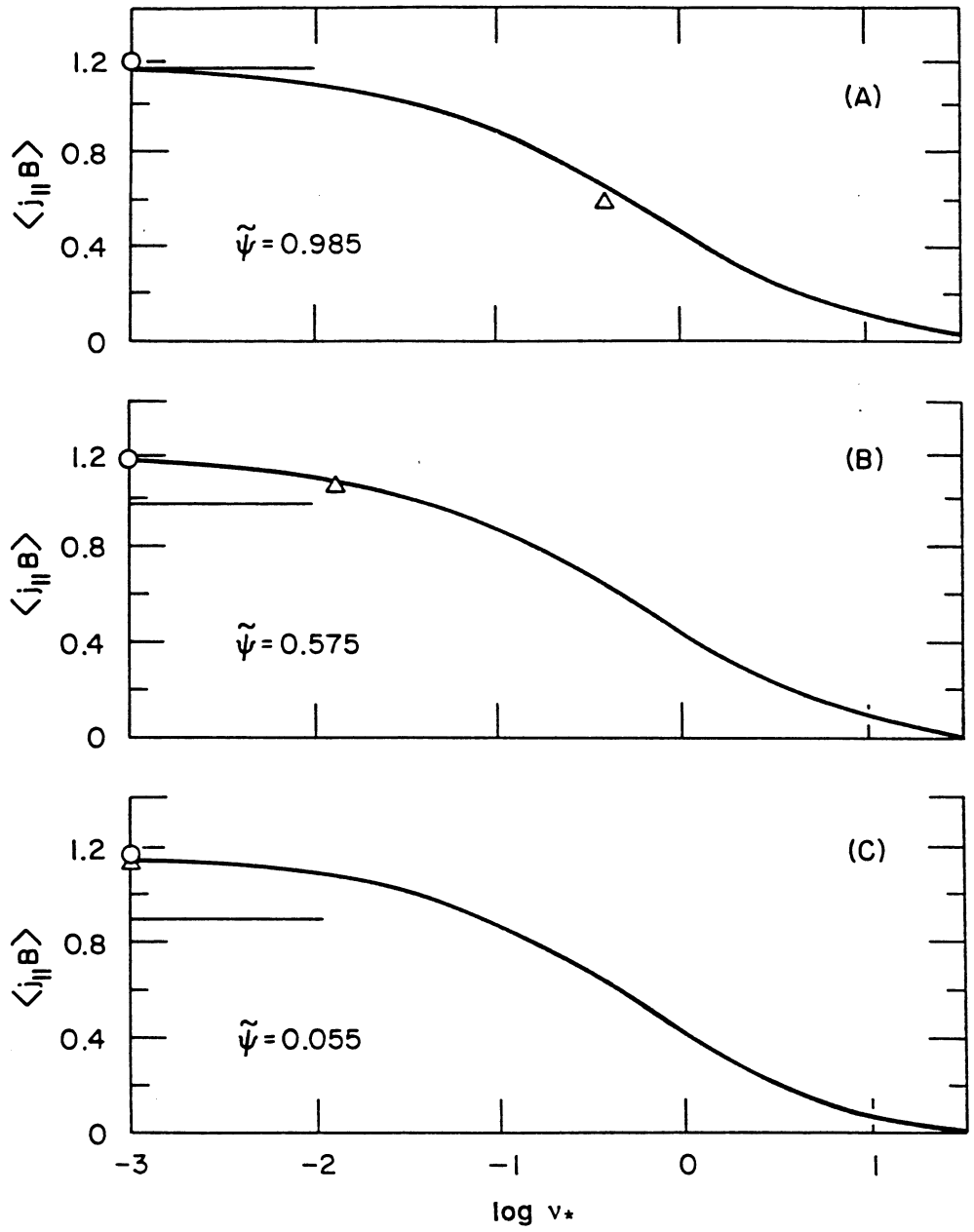

Figure 4.3-1. Average bootstrap-current density, $\langle j_{\|} B \rangle = \langle B^2 \rangle H(\psi)$, as a function of collisionality on three flux surfaces: (A) near magnetic axis, (B) at mid-plasma, and (C) near the edge. ARIES-I equilibrium with $\bar{n}_e \simeq 1.5 \times 10^{20}$ m^{-3}, $\bar{T}_e \simeq 22$ keV, and $Z_{eff} = 1.6$ is used but assuming $\nu_{*e} = \nu_{*i}$, and peaked density and flat temperature profiles ($\alpha_n = 1.3$, $\alpha_T = 0.1$). Horizontal lines are Hirshman's result (valid only for $\nu_* \to 0$), curves are from Hinton and Hazeltine formulation; triangles are Hinton and Hazeltine results at actual collisionality on each surface, plotted at $\nu_* \equiv (\nu_{*e} + \nu_{*i})/Z$, and open circles are Hinton and Hazeltine value in the limit $\nu_* = 0$.

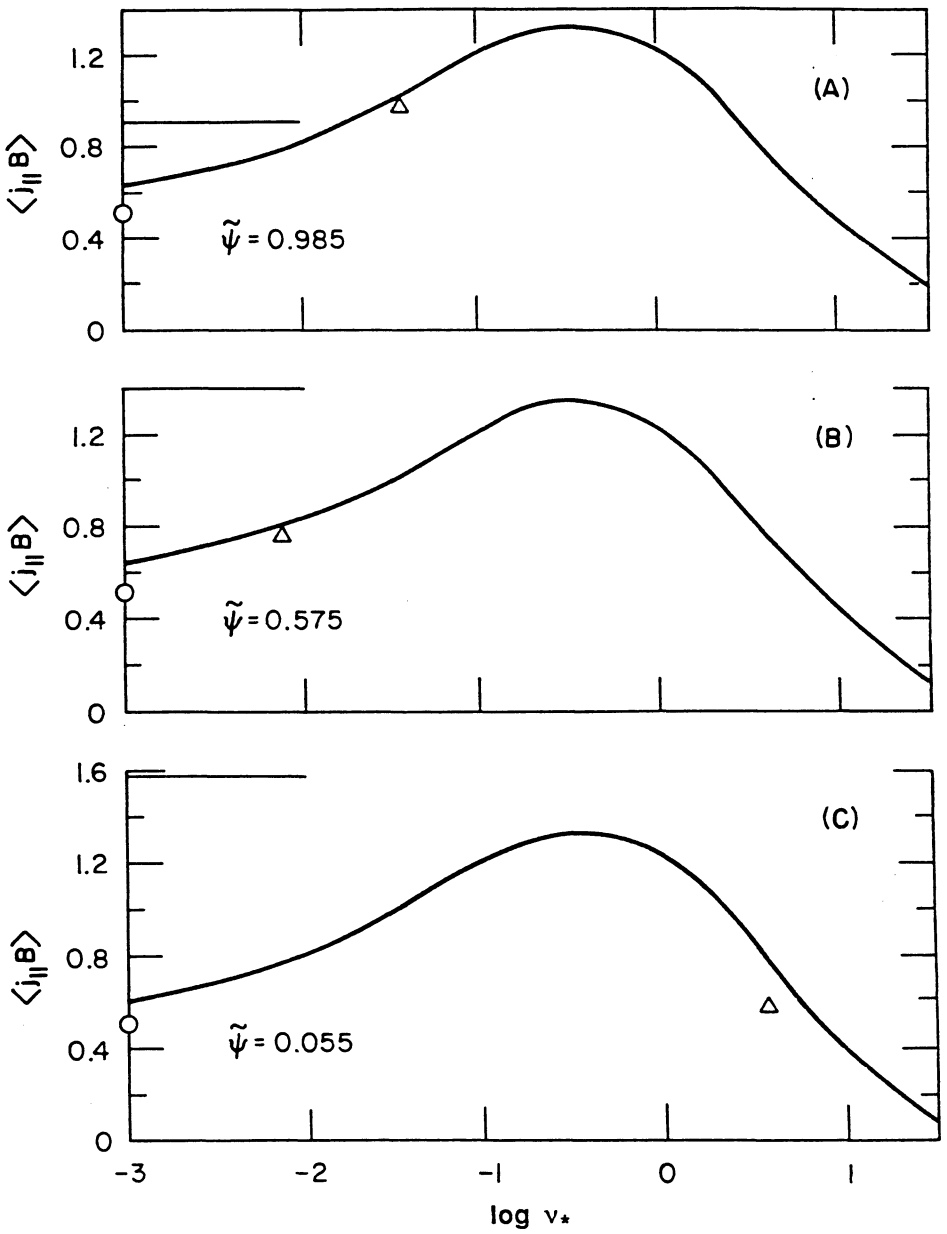

Figure 4.3-2. Average bootstrap-current density, $\langle j_{||} B \rangle = \langle B^2 \rangle H(\psi)$, as a function of collisionality on three flux surfaces: (A) near magnetic axis, (B) at mid-plasma, and (C) near the edge. ARIES-I equilibrium with parameters similar to those of Fig 4.3-1 are used with the exception of flat density and peaked temperature profiles ($\alpha_n = 0.05$, $\alpha_T = 1.35$). Horizontal lines are Hirshman's result (valid only for $\nu_* \rightarrow 0$), curves are from Hinton and Hazeltine formulation; triangles are Hinton and Hazeltine results at actual collisionality on each surface, plotted at $\nu_* \equiv (\nu_{*e} + \nu_{*i})/Z$, and open circles are Hinton and Hazeltine value in the limit $\nu_* = 0$.

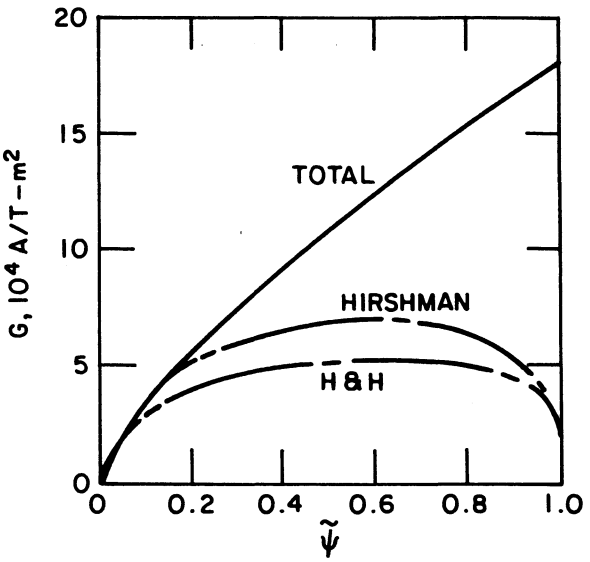

Figure 4.3-3. Comparison of two calculations of bootstrap contribution to $\langle j_{||} B \rangle$; total is the requirement for the ARIES-I reference equilibrium.

pellet fueling near the magnetic axis is unlikely. The reference equilibrium for ARIES-I has: pressure, $p(\psi) = p_o \tilde{\psi}^{\alpha}$, density, $n(\psi) = n_o \tilde{\psi}^{\alpha_n}$, and temperature, $T(\psi) = T_o \tilde{\psi}^{\alpha_T}$; with $\alpha = 1.4$, $\alpha_n = 0.3$, and $\alpha_T = 1.1$, where $\tilde{\psi}$ is the normalized poloidal flux (unity at the magnetic axis and zero at the separatrix). For comparison with BALDUR (1-D profiles), the plasma profiles are plotted *versus* the horizontal half width in Fig. 4.3-4. The pressure curve has been shown stable to ideal-MHD modes, and the temperature and density profiles are qualitatively similar to the transport code results. Based on studies with these profiles in the TRAC-II power-balance code and the ARIES-I systems code, it was determined to select the following operating points for ARIES-I:

$$
\begin{aligned}
T_{eo} &= 44.2 \text{ keV}, && \text{(volume-averaged } \bar{T}_e = 17.4 \text{ keV)} \\
T_{io} &= 43.5 \text{ keV}, \\
n_{eo} &= 1.85 \times 10^{20} \text{ m}^{-3}, && (\bar{n}_e = 1.33 \times 10^{20} \text{ m}^{-3}) \\
Z &= 1.6,
\end{aligned}
$$

with $\beta_t = 1.9\%$, $I_o = 11$ MA, Shafranov poloidal beta $\beta_I = 2.4$, and the ratio of peak-to-average pressures is $p_o/\bar{p} = 3.0$. In the absence of a bootstrap effect, the reference reactor would require $P_{CD} = 337$ MW for steady-state operation ($\gamma = 0.31$). With the bootstrap effect, only $P_{CD}^B = 100$ MW is needed ($\gamma^B = 0.98$), leading to $\Gamma = 0.68$. Although the ARIES-I parameters used in this set of calculations differ somewhat from the reference case in Table 4.1-I, the results should apply equally well to the reference case.

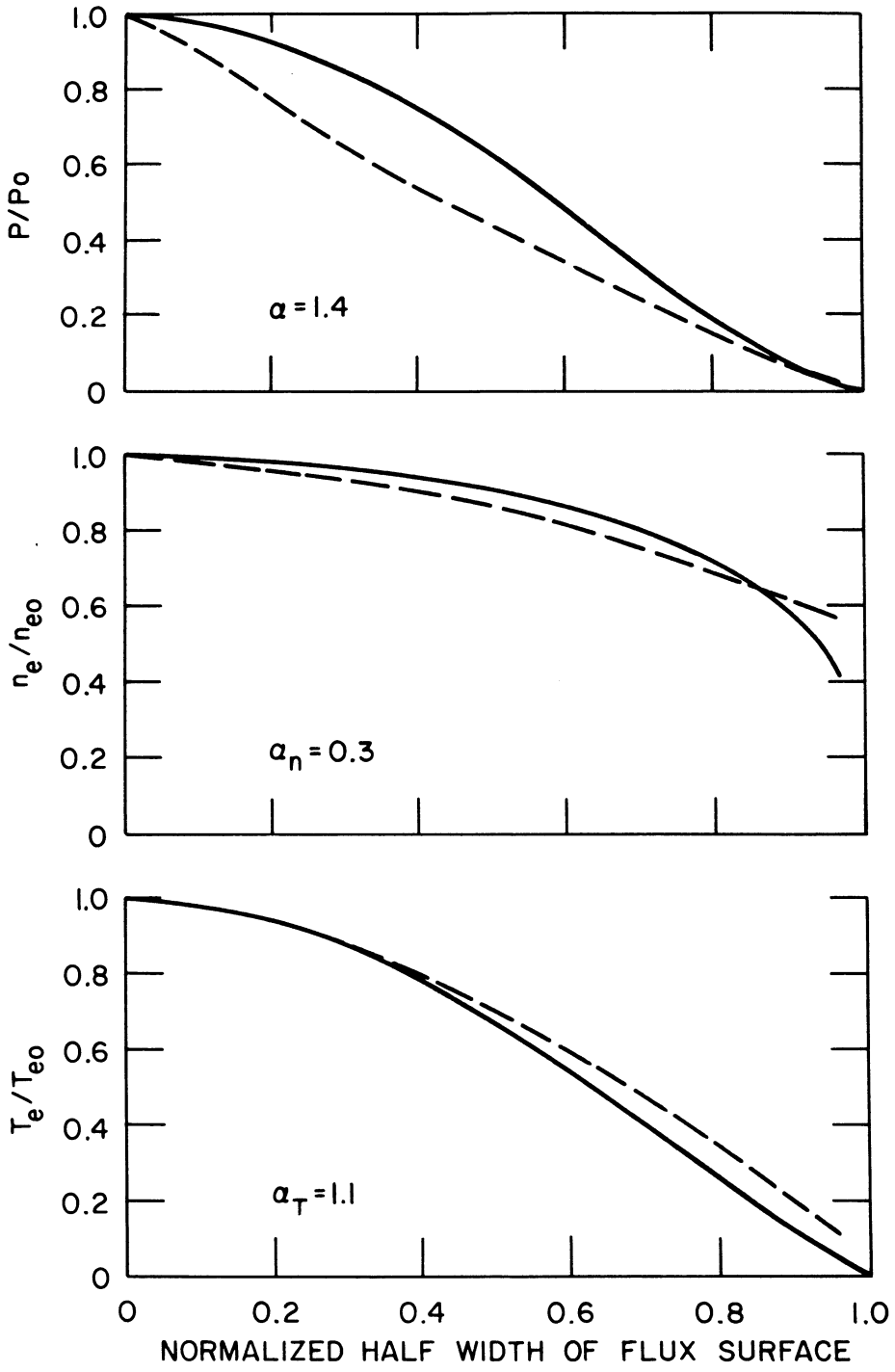

Figure 4.3-4. Normalized plasma (A) pressure, (B) density, and (C) temperature profiles. Dashed lines are typical 1-D BALDUR simulation results. Solid lines are from reference ARIES-I equilibrium.

4.4. PHYSICS OF FAST-WAVE CURRENT DRIVE

Fast-wave current drive (FWCD) is chosen as the reference current-drive technique for the ARIES-I design. This technique involves accelerating electrons by wave electric and magnetic fields along the field lines in the ion-cyclotron range of frequencies (ICRF). Although FWCD efficiency is considered moderate ($\gamma \sim 0.3$–0.4) for reactor applications and the data base is not extensive, FWCD is considered attractive mainly because of its modest technological requirements, high source efficiency, low unit cost ($1/W), and excellent integrability into the reactor environment. In this section, the experimental data base for FWCD is first reviewed and then a brief description of the theory, including various factors governing the current-drive efficiency, is given. In particular, a calculational model was developed during the course of this design study to account for efficiency degradation due to the presence of trapped electrons. This model is then incorporated into a fast-wave ray-tracing code that computes the RF-driven current profile with a given incident wave spectrum from the launchers. Coupled with an MHD equilibrium solver, which also calculates the bootstrap current, the ray-tracing code gives the required radio-frequency (RF) current-drive power for the reference ARIES-I parameters.

4.4.1. Experimental Status

There has been steady progress in the experimentation with FWCD. The experimental evidence for FWCD was extensively documented at the beginning of the ARIES-I study and detailed analyses can be found in Ref. [33]. The status as of 1988 can be summarized as follows:

- Antennas (waveguides and loops) have successfully launched the fast-wave polarization.
- Current drive depends on the directionality of the launched spectrum, as predicted.
- Current-drive results agree with the linear electron-damping theory in that the effect is largest at phase speeds on the order of the electron thermal speed.
- The ratio of driven-current to power at a fixed temperature fits the relationship $\bar{n}_e I_o R/P \equiv \gamma =$ constant, as predicted by theory.
- At low frequencies, for which the lower-hybrid resonance is not present in the plasma, FWCD occurs at densities much higher than are achievable with slow-wave (lower-hybrid) current drive, as predicted.

- At higher frequencies, FWCD is as good as slow-wave current drive, but possible coupling of fast-wave power to the slow-wave branch occurs.

The successful achievement of FWCD at densities in excess of the lower-hybrid limit is shown in Fig. 4.4-1. The additional advantage enjoyed by the fast wave is that the parallel index of refraction, $N_{||}$, may be sufficiently low such that the waves can penetrate to high temperatures ($T_e \gg 10$ keV), in contrast to lower-hybrid waves.

In the past year additional experiments have further validated the theory of FWCD:

- A direct comparison of slow- and fast-wave antennas on the same device (Irvine Torus) has demonstrated the superior performance of FWCD [34].
- Direct electron heating via transit-time magnetic pumping (TTMP) was shown for the first time with ICRF ($\sim$60 MHz) on JET [35].
- Spectral control with a four-loop antenna was shown and linear Landau damping and electron heating was confirmed with the fast wave on JFT-2M [36].

As discussed in detail in Ref. [33], the achievements of FWCD are beginning to rival those of slow-wave (lower-hybrid) current drive. They include:

- Gas breakdown and current start-up (Synchromak);
- Current ramp-up: $dI/dt = 0.3$ MA/s (JIPPTII-U);
- Density limit: $> 1.3 \times 10^{19}$ m^{-3} (Synchromak);
- Radio-frequency-driven current: 0.1 MA (JFT-2M);
- Efficiency: $\gamma = 0.04$ at 1 keV (JFT-2M).

On the basis of such increasing experimental support, it is evident that FWCD is a reasonable candidate for ARIES-I.

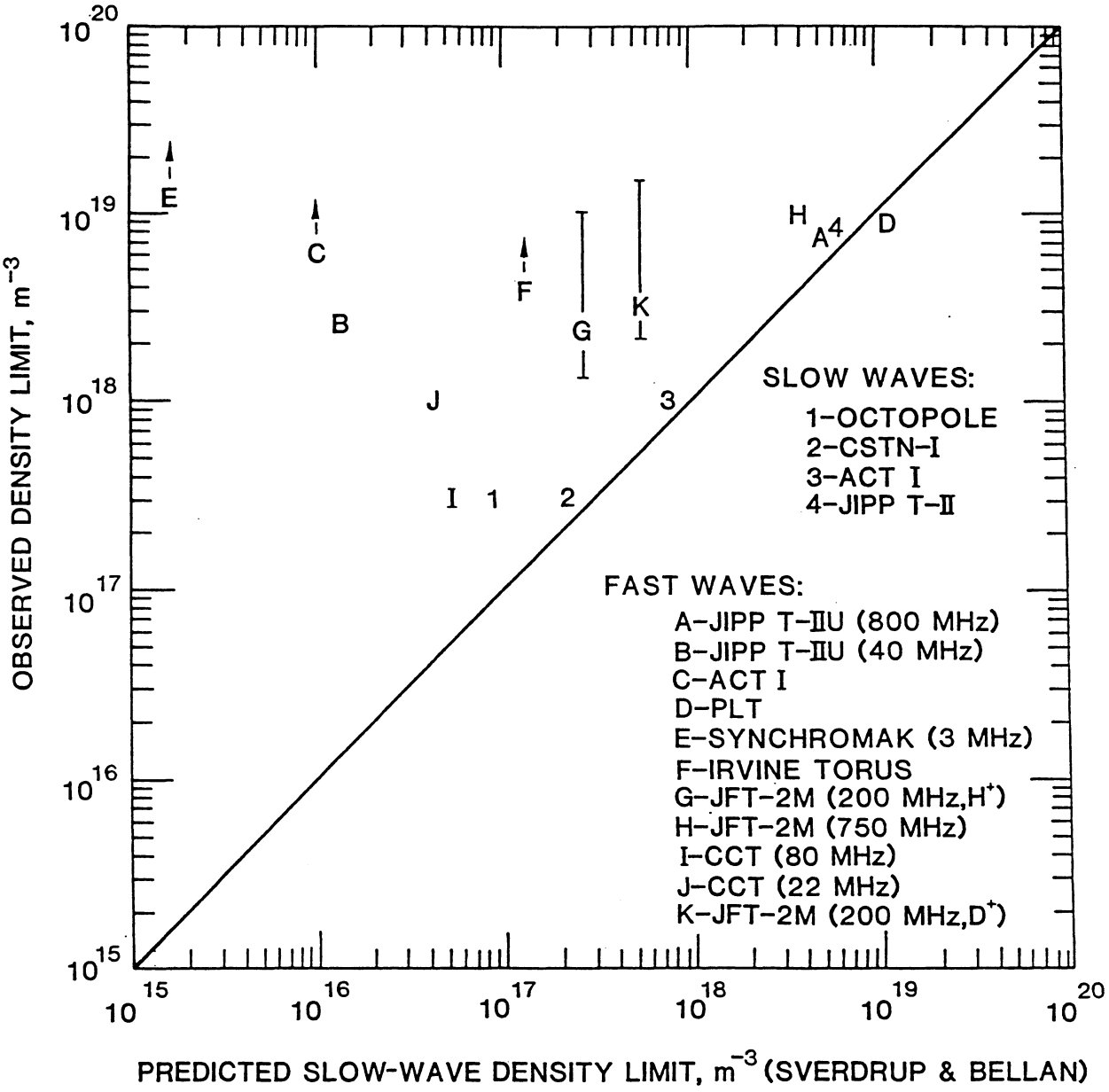

Figure 4.4-1. Comparison of slow- and fast-wave current-drive density limits [33].

4.4.2. Neoclassical Effects on RF Current Drive

In an axisymmetric tokamak in steady-state equilibrium, assuming there is no inductive electric field, the current density parallel to the magnetic field may be expressed [27] as $j_{||} = j_{||}^{PS} + B(G + H)$, where $j_{||}^{PS}$ is the well-known Pfirsch-Schlüter current (which is proportional to the pressure gradient) and B is the magnetic field strength. A goal of steady-state current drive is to arrange the contributions of the bootstrap current, H, and noninductive current, G, so that the resulting MHD equilibrium has desirable stability properties with a minimum amount of external driving power. Whereas the bootstrap current is caused by the neoclassical orbit effects associated with finite aspect ratio [32], it is clear that magnetic trapping will degrade the efficiency of generating current with fast waves.

In this section, an analytic expression is derived in order to provide a convenient function for accurate ray-tracing or full-wave calculations of RF current drive in realistic toroidal geometries. This analytic approach demonstrates that there are two principal neoclassical effects that act to diminish RF current-drive efficiency. For current drive at high phase speeds, typically achieved by Landau damping of lower-hybrid slow waves resonant at parallel velocities above the electron thermal speed ($v_e \ll \omega/k_{||}$), wave energy is added to electrons that are far from the trapped region of velocity space. These current carriers, however, will eventually diffuse via collisions until they become magnetically trapped and cease to provide a parallel electric current. On flux surfaces with a local inverse aspect ratio, $\epsilon \leq 0.1$, the current-drive efficiency is moderately reduced [37]. On the other hand, some waves, such as the low-frequency fast wave (compressional Alfvén wave), may resonate with low-phase-speed electrons via combined Landau damping and TTMP. Since these waves mostly add energy to electrons with low parallel velocities ($\omega/k_{||} \leq v_e$,) and over a range of large perpendicular velocities ($v_e \leq v_\perp$), they directly interact, to a great extent, with magnetically trapped electrons. As the wave phase speed ($\omega/k_{||}$) approaches zero, the current-drive efficiency is expected to vanish.

Both of the neoclassical effects discussed above are qualitatively derived in this section. However the derivation, which uses Giruzzi's response function [37], cannot be quantitatively accurate because of the high-energy approximation assumed for the electron collision operator. Therefore, in addition, the current-drive efficiency is computed by integrating the response function, which is computed numerically from the bounce-averaged adjoint equation in toroidal geometry [38]. These calculations are done for several values of ion charge, Z, inverse aspect ratio, ϵ, poloidal location where the wave heating occurs, θ, a large range of normalized phase speeds, $w \equiv \omega/k_{||}v_e$, and for both Landau damping and Alfvén-wave types of resonance. Relativistic corrections are on the

order of $\vartheta(T_e/m_ec^2)$ and are small for plasma electron temperatures ($T_e \leq 50$ keV) and for the waves considered, so only the nonrelativistic results are presented here. On a given poloidal flux surface, ψ, the RF-driven current contribution, G, is expressed as [27, 38]

$$G \equiv \frac{\langle j_{||}^{RF} B \rangle}{\langle B^2 \rangle} = \frac{V'}{2\pi q} \frac{\eta}{R} \langle p^{RF} \rangle , \tag{4.4-1}$$

where $j_{||}^{RF}$ is the RF-driven current density, $V' = dV/d\psi$ is the derivative of the toroidal volume, q is the safety factor, p^{RF} is the RF heating power density, and $\langle \cdot \rangle$ denotes the flux surface average. In this normalization, the current-drive efficiency, η, is related to a dimensionless function, $\tilde{\eta}$, as

$$\eta = \frac{19.2 \times 10^{18}}{ln\Lambda} \frac{T_e}{n_e} \tilde{\eta} , \tag{4.4-2}$$

where $ln\Lambda$ is the Coulomb logarithm, n_e is the local electron density, and SI units are used with the exception of temperatures which are in keV. By comparing the numerically determined $\tilde{\eta}$ with the analytic expression, it proves possible to select constants in the $\tilde{\eta}$ expression in order to closely fit the numerical values over the range studied. The final results, $\tilde{\eta}(Z, \epsilon, \theta, w)$, are functions of four variables for both wave types.

In addition to Giruzzi's work [37], there were earlier studies relevant to this problem. For current drive by Landau damping, an early account of trapping effects was provided by Cordey, Edlington, and Start [39], and more accurate results have been provided recently by the CQL computer code [40]. In both references, however, the bounce-averaged Fokker-Planck equation essentially assumes uniform flux-surface illumination by the RF so no explicit θ-dependence appears. For Alfvén-wave heating, even the published $\epsilon = 0$ results are inaccurate (*e.g.*, the Fokker-Planck calculation of Fisch and Karney [41] resulted in $\tilde{\eta}$ typically 20% smaller than the adjoint solution found here) and results for the $\epsilon = 0.1$ case in Ref. [42] are quantitatively correct only for $w \gg 1$ because electron-electron collisions were neglected.

In the semi-analytic calculation of $\tilde{\eta}$, velocity-space variables are selected that are local to the poloidal position on a flux surface, θ, where the RF heating occurs. The electron parallel- and perpendicular-velocity components are normalized to the thermal speed, $v_e \equiv (T_e/m_e)^{1/2}$, as $w = v_{||}/v_e$ and $x = v_\perp/v_e$, and its normalized speed is $u = (x^2 + w^2)^{1/2}$. If the maximum field amplitude on a flux surface is $B_M \equiv B(\psi, \pi)$ and the local field is $B = B(\psi, \theta)$, and defining

$$x_t \equiv w \left(\frac{B}{B_M}\right)^{1/2} \left(1 - \frac{B}{B_M}\right)^{-1/2} , \tag{4.4-3}$$

then electrons with $x < x_t$ are free to circulate along the field line, while electrons with $x_t < x$ are trapped and cannot contribute to $j_{||}^{RF}$ in a time-averaged sense. It is convenient to also define pitch angles $\lambda \equiv w/u$ and

$$\lambda_t \equiv \left(1 - \frac{B}{B_M}\right)^{-1/2} . \tag{4.4-4}$$

Then, trapped electrons have $0 \leq \lambda < \lambda_t$. Note that for circular flux surfaces at low beta and large aspect ratio, the field is given by $B \propto 1 - \epsilon \cos\theta$, where $\epsilon = r/R_o$. Then,

$$\lambda_t = 1 - \frac{1 - \epsilon\cos\theta}{1 + \epsilon} . \tag{4.4-5}$$

If the response function $\chi(w, x)$ is known at θ, then the normalized RF current density, $\tilde{j}$, is found by an integration over circulating-particle velocity space [43],

$$\tilde{j} = 2\pi \int_{-\infty}^{\infty} dw \int_0^{x_t} dx\, x\, \mathbf{S} \cdot \frac{\partial \chi}{\partial \mathbf{u}} , \tag{4.4-6}$$

where

$$\mathbf{S} \cdot \frac{\partial \chi}{\partial \mathbf{u}} = w\, D^{RF}\, f\, \frac{\partial \chi}{\partial w} , \tag{4.4-7}$$

assuming linear damping by waves that push electrons along the field lines so that the electron distribution remains Maxwellian: $f = \bar{f} e^{-u^2/2}$. The perpendicular velocity dependence of RF diffusion differs for Landau damping and Alfvén waves [41, 43]:

$$D^{RF} = D_o\, \delta\left(w - \frac{\omega}{k_{||}\, v_e}\right) \times \begin{cases} 1 & \text{Landau damping} \\ (2 - x^2)^2 & \text{Alfvén waves} \end{cases} , \tag{4.4-8}$$

where D_o is a constant and a narrow $k_{||}$ spectrum is assumed. Wave heating occurs for trapped as well as circulating electrons and the normalized heating-power density is given by

$$\tilde{p} = 2\pi \int_{-\infty}^{\infty} dw \int_0^{\infty} dx\, x\, \mathbf{S} \cdot \frac{\partial}{\partial \mathbf{u}} \left(\frac{u^2}{2}\right) , \tag{4.4-9}$$

where $\mathbf{S}$ is the RF-induced flux in velocity space, and

$$\mathbf{S} \cdot \frac{\partial}{\partial \mathbf{u}} \left(\frac{u^2}{2}\right) = w^2\, D^{RF}\, f . \tag{4.4-10}$$

Note that the velocity-space diffusion, **S**, is parallel to the magnetic field only at the positions θ, where the wave power is transferred to electrons. Although the RF-driven current and heating-power densities vary along a field line, it is proposed that the flux-surface-averaged efficiency is given by the ratio of the local quantities in Eqs. (4.4-6) and (4.4-9) as

$$\tilde{\eta} \;=\; \tilde{j}/\tilde{p}\,. \tag{4.4-11}$$

Use of the approximate response function of Giruzzi [37],

$$\chi \;=\; \left[1-\left(\frac{\lambda_t}{\lambda}\right)^{\alpha}\right]\frac{2w\,u^3}{5+Z}\,, \tag{4.4-12}$$

results in the following partial derivative in Eq. (4.4-7):

$$\frac{\partial\chi}{\partial w} \;=\; \left[1-\left(\frac{\lambda_t}{\lambda}\right)^{\alpha}\right]\frac{2(3uw^2+w^3)}{5+Z}+\frac{2}{1+Z}\left(\frac{\lambda_t}{\lambda}\right)^{\alpha}x^2\,u\,. \tag{4.4-13}$$

For a straight magnetic field ($\lambda_t \equiv 0$), Eq. (4.4-13) reduces to the well-known Fisch-Boozer result [44]. The derivation of this expression assumed that wave energy is transferred to high-energy electrons, which is a good approximation at $w \gg 1$. At low phase speeds ($w \leq 1$), this condition can be mildly satisfied (*e.g.*, for Alfvén-wave damping at $\epsilon = 0$), since the RF diffusion due to Alfvén waves is dominated by electrons at $x \geq 1$. For $\epsilon \neq 0$, however, the assumption is violated at $w \ll 1$ since only electrons with $x < 1$ are free to carry current. As will be seen, Eq. (4.4-13) nevertheless results in the correct functional dependence of $\tilde{\eta}$ for $\epsilon \leq 0.1$ and $w \geq 0.2$. The next step is to evaluate $\tilde{\eta}$ in the two phase-speed limits and then seek a uniform approximation over the full range of w.

At high phase speeds the exponential dependence, $f \propto e^{-x^2/2}$, cuts off the integrals at large x so the approximation $x \ll w$ can be used. Then $u \simeq w$ in the first term of Eq. (4.4-13) and the second term can be neglected. The resulting efficiency at $w \gg 1$ is given by

$$\tilde{\eta} \;\simeq\; \lim_{w\gg 1}\left(\frac{\partial\chi/\partial w}{w}\right) \;\simeq\; \left[1-\left(\frac{\lambda_t}{\lambda_r}\right)^{\alpha}\right]\frac{8w^2}{5+Z}\,. \tag{4.4-14}$$

The pitch angle at $\lambda_r \equiv w/u_r$ has been evaluated with $u_r \equiv (x_r^2+w^2)^{1/2}$, where x_r is a constant. Giruzzi suggests evaluating λ_t for these circulating electrons at an "averaged" value of θ, so $\lambda_t \sim \epsilon^{1/2}$, and he finds the exponent $\alpha = (5+Z)/(1+Z)$, which approaches unity as Z becomes large. In order to match the numerical results for $\tilde{\eta}$, Eq. (4.4-14) is replaced with $\tilde{\eta} \simeq R_c(\epsilon, w)\,\eta_o(Z, w)$, where

$$R_c \;=\; 1-\frac{\epsilon^n\,(x_r^2+w^2)^{1/2}}{\epsilon^n\,x_r+w}\,, \tag{4.4-15}$$

and in the $w \gg 1$ limit,

$$\eta_o \rightarrow \frac{8w^2}{5+Z}. \tag{4.4-16}$$

The function R_c is a generalization that qualitatively agrees with previous calculations [37, 39, 40] that show a reduction in $\tilde{\eta}$ for $\epsilon \neq 0$ at $w \gg 1$ (assuming x_r and ϵ^n are of order unity), but which also behaves as $R_c \rightarrow (w/\epsilon^n x_r)$ as $w \rightarrow 0$. This small-w behavior of R_c, which has not been derived, will be required in order to reproduce the correct w-dependence of $\tilde{\eta}$ when $w \leq 1$ and $\epsilon \neq 0$. The exponent n will be determined by comparison with the numerical results.

In the low phase-speed limit, the evaluation of $\tilde{\eta}$ requires explicit integrations over x for $\tilde{p}$ and $\tilde{j}$; the integral for $\tilde{p}$ is straightforward, while the endpoint, x_t, of integration plays a dominant role in $\tilde{j}$. Since $D^{RF}(x)$ differs for Landau damping and Alfvén-wave heating, the two wave types are treated separately. Considering Landau damping first, we set $u = w$ and $\lambda = w/x$ when $w \ll 1$, and substitute both terms of Eq. (4.4-13) into Eq. (4.4-6). The result is an expression for $\tilde{j}$ involving functions of the form

$$I(p, x_t) = \int_0^{x_t} dx\, x^{p+1}\, e^{-x^2/2}. \tag{4.4-17}$$

To simplify matters, we replace $I(p, x_t)$ with a monotonic function of x_t, which preserves the correct values in both the large and small x_t limits, *i.e.*,

$$I(p, x_t) \simeq 2^{p/2}\,\Gamma\left(\frac{p+2}{2}\right)\left\{1 - \exp\left[-b(p)\left(\frac{y_t}{2}\right)^{(p+2)/2}\right]\right\}, \tag{4.4-18}$$

where

$$y_t \equiv x_t^2 = \frac{(1-\lambda_t^2)\,w^2}{\lambda_t^2}, \tag{4.4-19}$$

$$\frac{1}{b(p)} \equiv \frac{p+2}{2}\,\Gamma\left(\frac{p+2}{2}\right), \tag{4.4-20}$$

and $\Gamma(z)$ is the gamma function. Comparing the various contributions to $\tilde{\eta}$, it is seen that terms proportional to w^2 are generally negligible, and an adequate approximation to the result is

$$\tilde{j} = \frac{6\sqrt{2}\,\pi^{3/2}}{5+Z}\, D_o\, \bar{f}\, w\, e^{-w^2/2}\, C(\epsilon, \theta, w)\, M(\epsilon, \theta, w), \tag{4.4-21}$$

where

$$C = 1 - e^{-(c_o\, y_t)^m}, \tag{4.4-22}$$

$$M = 1 + A_o \left(\frac{\lambda_t}{w}\right)^k. \tag{4.4-23}$$

Dividing this by $\tilde{p}$, the low phase-speed limit,

$$\tilde{\eta} \;=\; \eta_o(Z,w)\, C(\epsilon,\theta,w)\, M(\epsilon,\theta,w)\,, \tag{4.4-24}$$

is obtained where, for $w \ll 1$,

$$\eta_o \;\rightarrow\; \frac{K}{w}\,. \tag{4.4-25}$$

The theoretical value of K is $3\sqrt{2\pi}/(5+Z)$, which yields the correct asymptotic Landau-damping form for η_o only in the Lorentz gas limit ($Z \gg 1$). The actual value should be $K = 3\sqrt{2\pi}/Z$ [39]. When $\epsilon \neq 0$ and $\theta \neq \pi$, the factor C severely cuts off the current-drive efficiency at small w, with the corresponding Landau-damping calculation having $m = 2.5$ and $c_o = 0.31$. In the factor M, which is expected to be of order unity for $w \geq 1$, both A_o and k ($= \alpha$) are functions of Z, but this Z variation will be suppressed in the approximate expression for $\tilde{\eta}$. All the constants in Eqs. (4.4-22) through (4.4-25) will be adjusted to fit the numerical results for $\tilde{\eta}$ at $Z = 1.0$ and 2.0.

The derivation of $\tilde{\eta}$ for Alfvén-wave damping in the $w \ll 1$ limit follows a similar procedure with the appropriate $D^{RF}(x)$ from Eq. (4.4-8) in both the $\tilde{p}$ and $\tilde{j}$ integrals. The functions for $\tilde{\eta}$ are identical to Eqs. (4.4-22) through (4.4-25) except the constants differ from the Landau-damping values. For example, one finds $K = 65.8/(5+Z)$ which differs from the correct Alfvén-wave asymptotic result [43] of roughly $K = 30/(0.678+Z)$. Because fewer collisional electrons at larger x are carrying the RF current, K is of course larger for Alfvén-wave than for Landau damping. By the same token, the detrimental effects of trapping set in more quickly for Alfvén-wave damping as w is reduced, resulting in a larger $m = 4.5$, with $c_o = 0.21$. In the factor M, the exponent k should be the same as for Landau damping, but the coefficient A_o is calculated to be larger for Alfvén-wave current drive.

Since C and M approach unity for large w, a uniform approximation to the efficiency,

$$\tilde{\eta} \;=\; C\, M\, \eta_o\, R_c\,, \tag{4.4-26}$$

is made. The straight-field efficiency, η_o, must agree with the limiting forms in Eqs. (4.4-16) and (4.4-25), so the following function is adopted:

$$\eta_o \;=\; \frac{K}{w} + C_o + \frac{8w^2}{5+Z}\,. \tag{4.4-27}$$

It is expected that the value of C_o will depend on Z. Although an analytic expression for $C_o(Z)$ is suggested in Ref. [43], the method here is to select both $K(Z)$ and $C_o(Z)$

to compare with the numerical results computed for the cases with $\epsilon = 0$. To this end, a series of numerical solutions for $\tilde{\eta}$ were computed, and the analytic function was fitted to the numerical results with the various constants given in Table 4.4-I. The analytic function agrees to within $\pm 12\%$ of the numerical result over the range of interest: $w > 0.5$, non-negligible $\tilde{\eta}$ (> 6), $0 \leq \epsilon \leq 0.25$, $Z = 1$ and 2, both wave polarizations, and most θ. The exception is for $\theta = 3\pi/4$, $\epsilon = 0.01$ for the Alfvén wave at $w \simeq 0.5$, where the error is in excess of 40%; this inaccuracy occurs where $\tilde{\eta}$ is a fast-varying function of θ and w and is acceptable for ray tracing in which the actual current generation is due to a broad range of w and θ values.

The analytic function, $\tilde{\eta}(\epsilon, \theta, w, Z)$, is compared with the numerical results for Landau damping in Fig. 4.4-2. Since Landau damping is only important at $w \geq 1$ (wave damping occurs before $w \leq 1$ is reached), the agreement is seen to be quite satisfactory. Note that $\tilde{\eta}$ is essentially independent of θ for Landau damping. The reduction of $\tilde{\eta}$ with increasing ϵ, including the calculated values at $\epsilon = 0.25$, from the CQL code [40]) is substantial.

Figure 4.4-3 shows that, for the same $Z = 1.0$, the Alfvén wave has a larger $\tilde{\eta}$ than Landau damping when $\epsilon = 0$ or $\theta = \pi/2$. In realistic situations ($\epsilon \neq 0$, $\theta < \pi/2$), the

Table 4.4-I.
Constants in the Analytic Fitting Function for $\tilde{\eta}$

	Landau-Damping Case	Alfvén-Wave Case
K	$6.0/Z$	$23.83/(0.678+Z)$
$(Z^{0.707})C_o$	7.67	8.27
n	0.77	0.77
x_r	3.5	3.5
m	1.38	2.48
c_o	0.389	0.0987
k	3.0	3.0
A_o	0.0	12.3

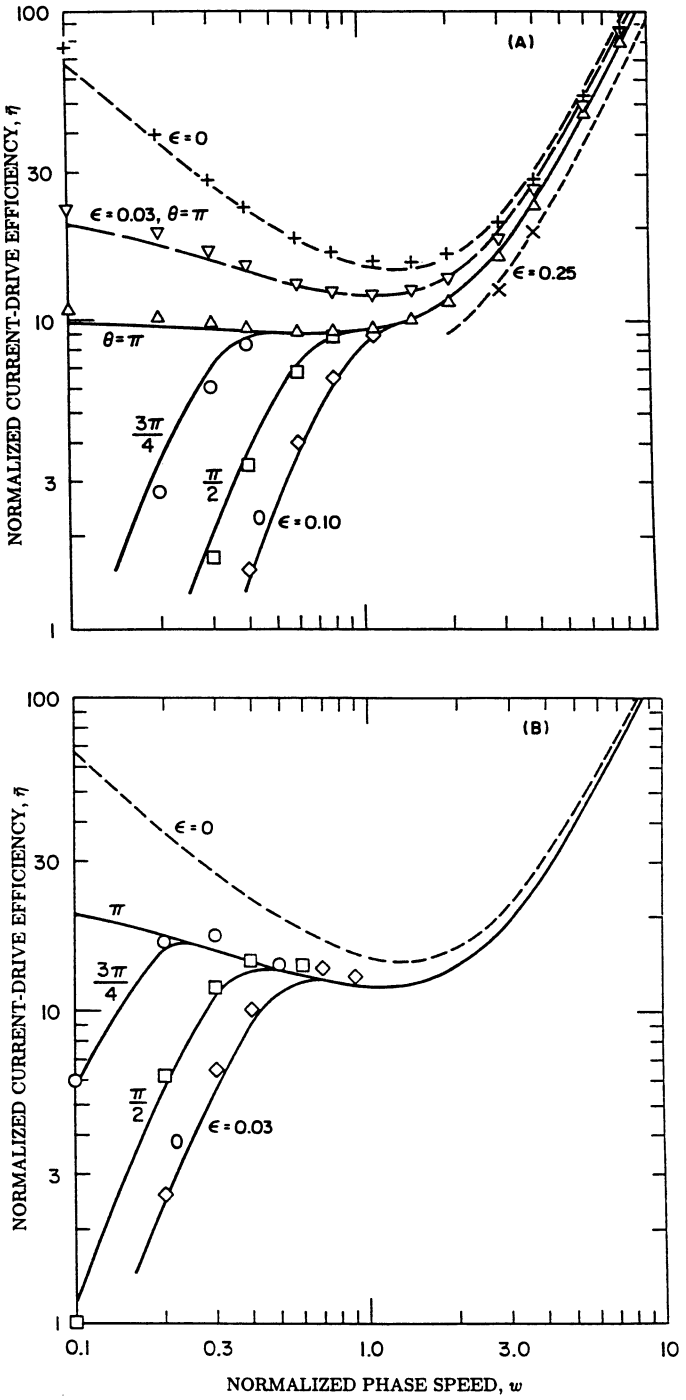

Figure 4.4-2. Normalized current-drive efficiency as a function of normalized parallel phase speed for Landau damping and $Z = 1.0$ at four different poloidal angles for: (A) $\epsilon = 0.10$ and (B) $\epsilon = 0.03$. The impact of $\epsilon \rightarrow 0$ at $\theta = \pi$ is also shown. Curves are analytic fits and points are numerically derived.

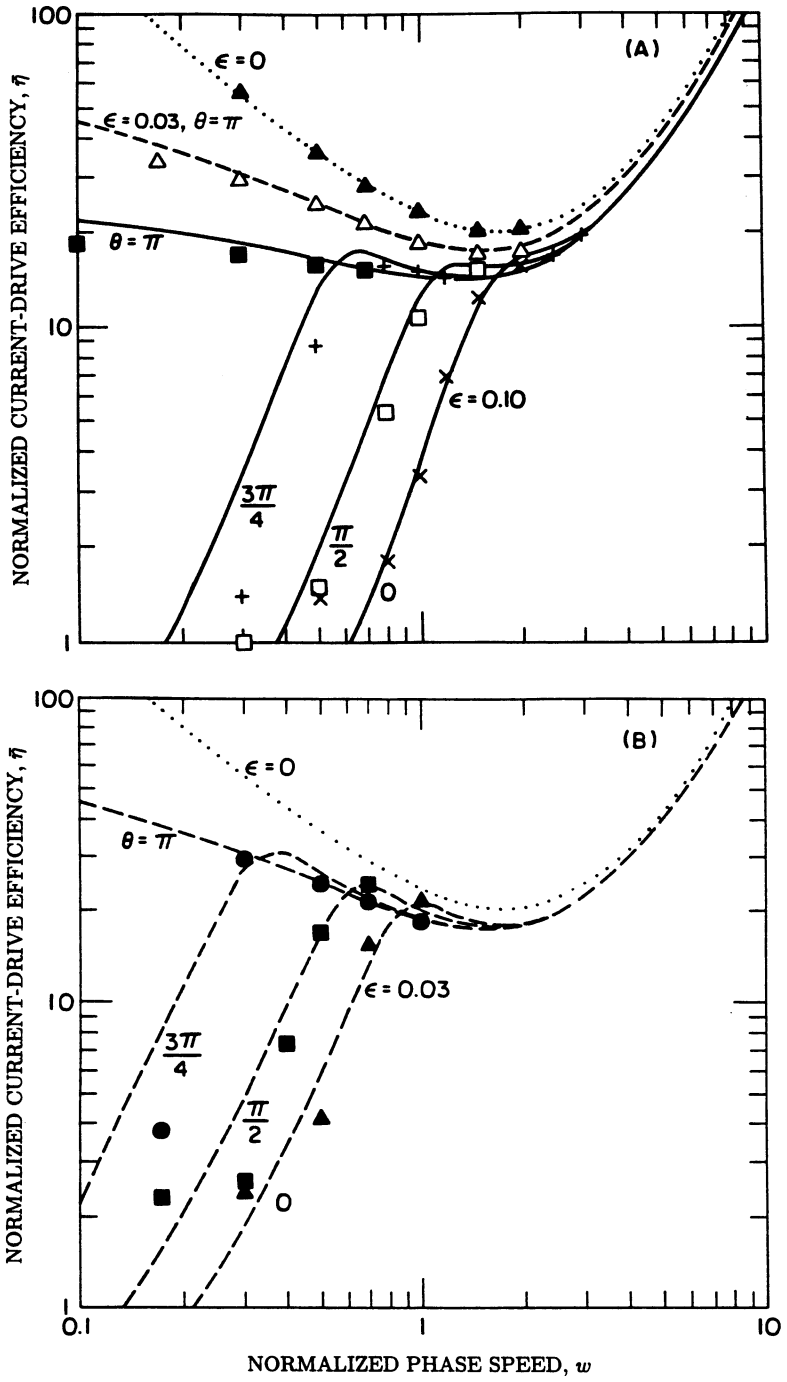

Figure 4.4-3. Normalized current-drive efficiency as a function of normalized phase speed for Alfvén wave and $Z = 1.0$ at four different poloidal angles and for: (A) $\epsilon = 0.10$ and (B) $\epsilon = 0.03$. The impact of $\epsilon \rightarrow 0$ at $\theta = \pi$ is also shown. Curves are analytic fits and points are numerically derived.

Alfvén-wave result is, however, smaller than the Landau-damping value when $w \leq 1$. Since ray tracing shows that Alfvén-wave current drive is dominated by $w \leq 2$, it is important to select spectra and launch positions such that $w \geq 1$ for FWCD. Finally, Fig. 4.4-4 shows a significant reduction of efficiency with Z, underscoring the desirability of maintaining a low impurity content. Overall, the analytic and numerical Alfvén-wave results are seen to be in good agreement over the important range $1.0 \leq w \leq 2.0$.

4.4.3. Effects of Transit-Time Magnetic Pumping

The final modification to the RIP code made it possible to determine whether a ray was in the Landau-damping or transit-time magnetic-pumping (TTMP) regime at each point in its trajectory. In the Landau-damping case, electrons are pushed by the wave electric field, $\tilde{E}$, while in the case of TTMP, they are accelerated by the $\mu \nabla \tilde{B}$ force, where μ is the magnetic moment and $\tilde{B}$ is the wave magnetic-field strength. The total force that is parallel to the ambient magnetic field on a electron guiding center is then

$$F_z = -e\,\tilde{E}_z - \mu \cdot \frac{\partial \tilde{B}_z}{\partial z}\,, \tag{4.4-28}$$

where z denotes the parallel direction and e is the electron charge. A discussion of how the corresponding quasi-linear diffusion coefficient is constructed is given in Ref. [41].

It is important to understand that the wave magnetic force on the guiding center is only important at high temperatures and rather low frequencies, so the functional dependence of F_z on these parameters must be included in the calculations. Algebraic analysis of the plasma dispersion relation reveals that F_z can be expressed as

$$F_z = \frac{e}{\omega_{ce}} \frac{\partial B_z}{\partial z} \left[\left(\frac{c^2 \omega^2}{\omega_{pi}^2} W + \frac{T_e}{m_e} \right) - \frac{v_\perp^2}{2} \right], \tag{4.4-29}$$

where

$$W \simeq \frac{Y + (\omega^2/\omega_{ce}\,\Omega_i)}{Y^2 + 4\pi\,\xi_{oe}^6\,\exp(-\xi^2)}\,, \tag{4.4-30}$$

$$Y \equiv 2\xi_{oe}^2(2\xi_{oe}\,\Theta - 1)\,, \tag{4.4-31}$$

and Θ is the plasma dispersion function. In this expression Ω_i is the ion cyclotron frequency, ω_{pi} is the ion plasma frequency, and

$$\xi_{oe} = \frac{\omega}{\sqrt{2}\,k_{||}\,v_e} = \frac{w}{\sqrt{2}}\,. \tag{4.4-32}$$

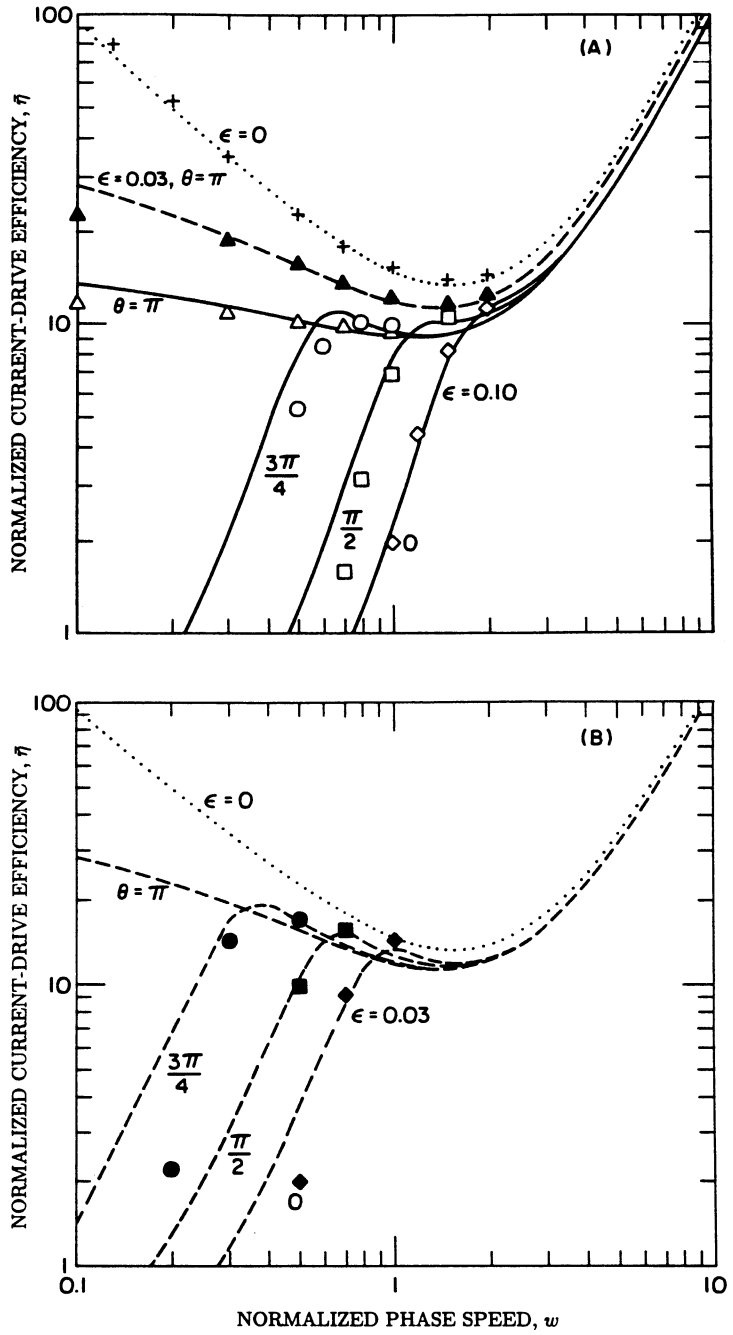

Figure 4.4-4. Normalized current-drive efficiency as a function of normalized parallel phase speed for Alfvén wave and $Z = 2.0$ at four different poloidal angles and for: (A) $\epsilon = 0.10$ and (B) $\epsilon = 0.03$. The impact of $\epsilon \to 0$ at $\theta = \pi$ is also shown. Curves are analytic fits and points are numerically derived.

In the linear limit, current drive is independent of the amplitude of F_z but sensitive to the $v_\perp$-dependence of F_z; in particular, the point at which $F_z(v_\perp)$ is zero is important. With reasonable accuracy, once can replace W with unity, and the result is that TTMP dominates the current drive for Alfvén wave (*i.e.*, $F_z = 0$ at $v_\perp \leq v_e$ when $\omega^2/\omega_{pi}^2 \leq v_e^2/c^2$). In the RIP code, an interpolation between the Landau-damping and Alfvén-wave current-drive efficiencies is used, based on the ratio of these parameters; the plasma quantities are explicitly calculated at each point along the ray path.

4.4.4. Base Scenario for ARIES-I

The plasma parameters and profiles were described in Sec. 4.3.3; this section outlines the selection of the current-drive parameters needed to provide the seed current for the stable equilibrium. It is noted that the majority of the parameters used in this section (*e.g.*, $R = 7.25$ m, $a = 1.61$ m, $B_c = 21.2$ T, $B_o = 11.7$ T, $I_p = 11.0$ MA, $q_* = 3.3$, and the n_e and T_e profiles as given in Sec. 4.3.3) differ from those in Table 4.1-I for the reference ARIES-I. The results, however, should apply well for the reference case.

The first issue is the choice of wave frequency, f, and a variety of trade-offs must be considered. Although FWCD is possible with frequencies from ~10 MHz to ~10 GHz, a frequency of 148 MHz was selected with a source tunable to 170 MHz for auxiliary heating, after considering the following points:

- Below the fundamental ion-cyclotron frequency, electron damping is weak, requiring multi-pass absorption. Such weak damping inhibits the ability to control the current profile. For $f \geq 150$ MHz, desirable single-pass absorption occurs.
- At high frequencies (≥ 800 MHz), the fast wave might couple to the lower-hybrid slow wave, preventing current drive at the magnetic axis.
- In the range ~60–200 MHz, strong fuel ion-cyclotron damping may occur at discrete frequencies. At $f \leq 50$ MHz, there is no ion interaction, while above 200 MHz, energetic α-particle damping becomes dominant [25]. Figure 4.4-5 shows that $f = 148$ MHz removes the second-harmonic fuel resonances into the cold plasma edge, which results in negligible ion damping. It is also seen that $f = 170$ MHz allows second-harmonic deuterium or proton-minority heating to ignition.
- Coupling to the ion Bernstein wave may be a problem at moderate harmonics of the cyclotron frequency [40], which is another reason to avoid $f \sim 200$–500 MHz.

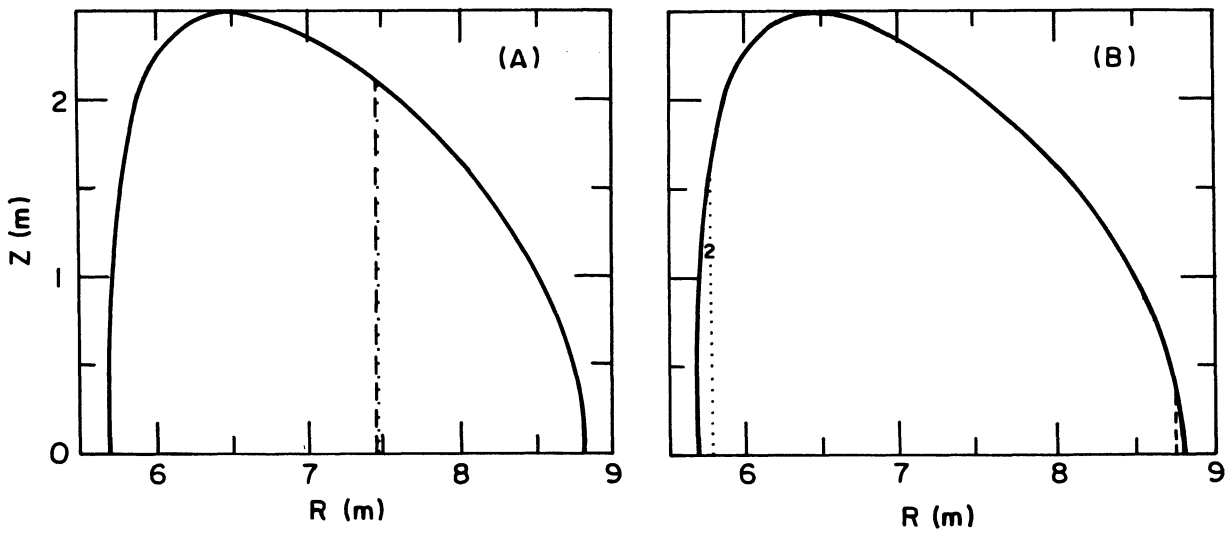

Figure 4.4-5. Ion-cyclotron resonance locations for (A) proton-minority heating at 170 MHz and (B) electron current drive at 148 MHz.

- Supra-thermal α-particles strongly absorb the fast wave through Doppler-shifted higher-harmonic resonances for $f \leq 800$ MHz [25].

The second issue in FWCD relates to the launcher location. Outboard launch is evidently preferable in terms of ease of engineering and integration into the blanket and reactor structure. However, to maximize current profile control, it is desirable to absorb significant FWCD power off axis and locating the FWCD launcher somewhat above the mid-plane is helpful. Figure 4.4-6 shows five fast-wave rays emanating from the launcher at heights up to $\sim$1.6 m above the equatorial plane, and two lower-hybrid rays launched from the mid-plane region.

The poloidal mode-number power spectrum is also a factor to be considered. The rather localized position of the antenna dictates a broad poloidal spectrum and fairly high mode numbers are included in the ray-tracing calculation, as suggested by the antenna-coupling calculations [45]. To a larger extent, the poloidal mode numbers can be controlled by introducing a phase shift between two poloidally stacked modules, as outlined in Sec. 4.5.

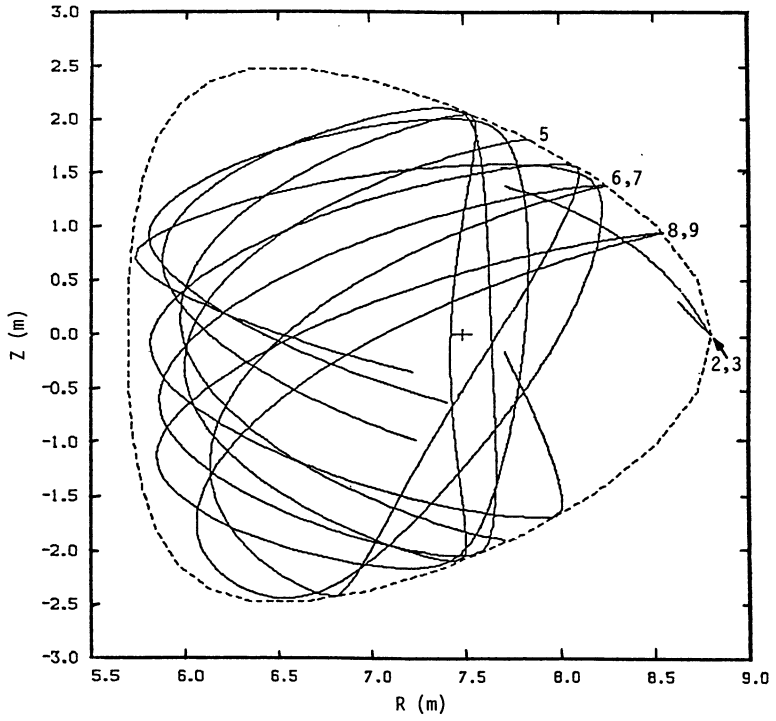

Figure 4.4-6. Ray trajectories of 148-MHz fast wave ($N_{||} \simeq 2.0$) for current drive launched above mid-plane (#5–9), and strongly damped lower-hybrid rays (8.0 GHz) launched at mid-plane (#2,3).

The final issue is the selection of the spectrum in $N_{||}$. Test rays were launched with many incident $N_{||}$ values in order to assess the spatial damping patterns and current-drive efficiency. It was found that the current-drive efficiency is quite insensitive to $N_{||}$ over a broad range ($\sim$1.5–2.5). The converged RF and MHD equilibrium solution, shown in Fig. 4.4-7, uses five fast-wave rays to represent a continuous power spectrum; additional lower-hybrid power (8.0 GHz) is supplied to provide the current density near the edge. As shown, the bootstrap effect contributes greatly to the result.

The final solution used 100.1 MW of FWCD power launched into the torus. The ray calculations were stopped with 6.9 MW of power left, so actually less than 100 MW was used for current drive. The central temperature was $T_{eo} \simeq 44$ keV, so the electron target plasma is mildly relativistic near the axis. Based on Ref. [43], the normalized current-drive efficiency is expected to be slightly increased by a factor of $\sim 1 + (T_{eo}/mc^2)$ and, if this credit is taken, it is expected that only $P_{FW} \simeq 92$ MW is needed for ARIES-I. The lower-hybrid power, $P_{LH} \simeq 5$ MW, is quite small, with a spectrum centered near the accessibility limit, $N_{||} = 1.4$.

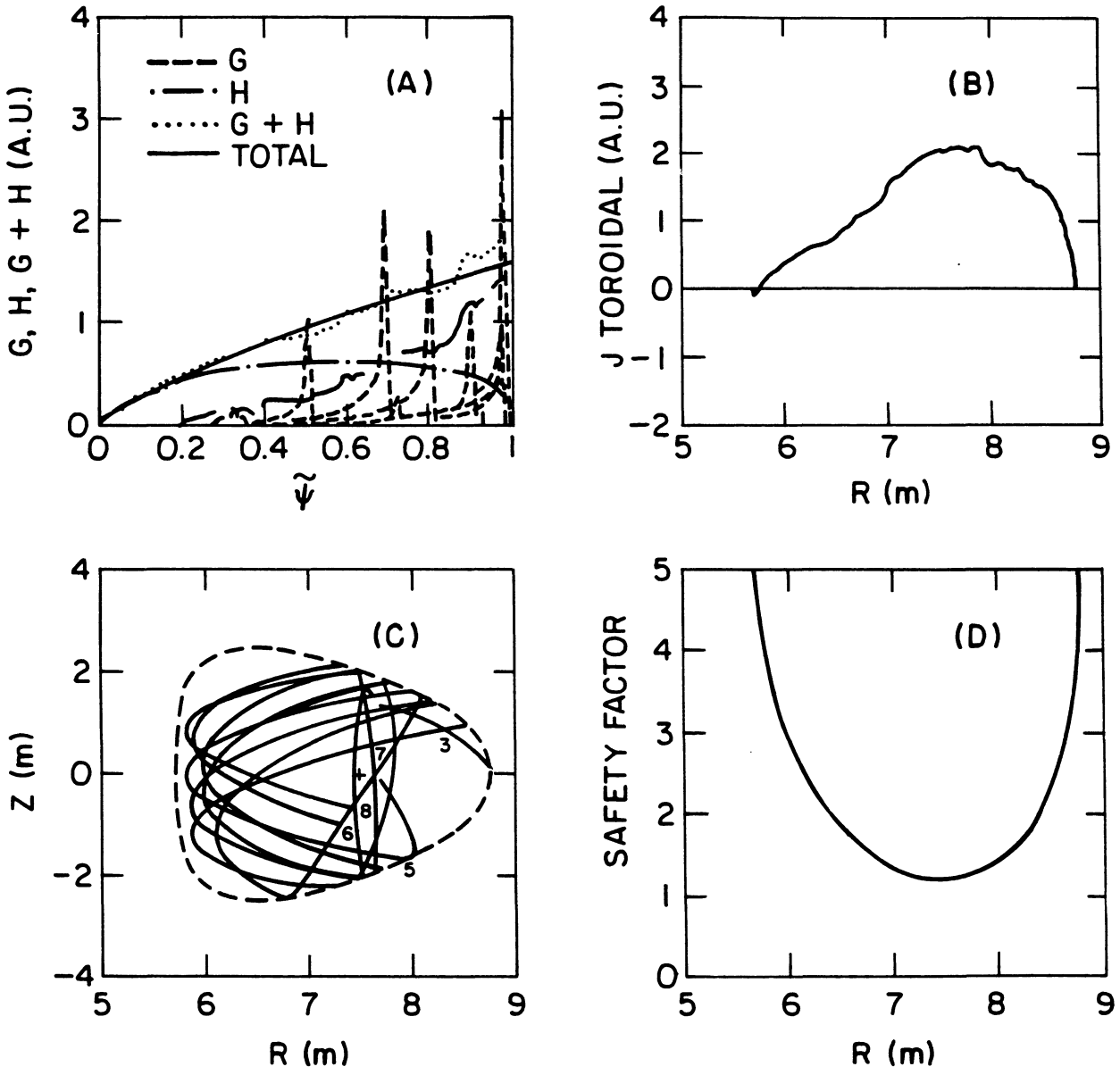

Figure 4.4-7. Converged, stable ARIES-I equilibrium with FWCD and bootstrap contribution: (A) Current profile contributions from fast wave, G, bootstrap effect, H, and the sum of $G + H$; (B) Toroidal current profile at mid-plane; (C) Projection of five rays (#3: lower-hybrid; #5–8: fast wave) onto minor cross section; and (D) Safety-factor profile at mid-plane.

4.4.5. Critical Issues

Throughout this study, a number of areas needing investigation have been identified with regard to FWCD for steady-state tokamaks. These are:

- Detailed studies of α-particle damping of the FWCD, including spatial and velocity distributions of the α-particles;
- Comparison of ray-tracing and full-wave calculations at low (ICRF) frequencies;
- Pressure profile control, in conjunction with current profile tailoring, which may allow access to higher stable Troyon ratios;
- Fast-wave current-drive experiments (*e.g.*, on DIII-D or JET) at $T_{eo} \geq 5$ keV;
- Upgrading the RIP code to include inductive currents, which will allow start-up and transformer-recharge simulations, in addition to bootstrap-current generation.

4.5. FAST-WAVE CURRENT-DRIVE SYSTEM

The ARIES-I design uses fast waves in the ion-cyclotron range of frequencies (ICRF) to drive the current, in addition to the naturally occurring bootstrap component. The frequency considered ($f = 141$ MHz) is close to that which commonly has been used in ICRF heating experiments to date ($f < 100$ MHz), so that only modest extrapolation from present technology is foreseen as necessary. The current-drive system consists of the radio-frequency (RF) source or generator, transmission line, phase-shift circuit, matching system, and the launcher which interfaces with the plasma. In this section, a description of the various component designs is given. The performance of these components dominates the overall system efficiency which, in turn, determines the amount of recirculating power in the reactor. Because the main goal of the design is to minimize this recirculating power, special emphasis is placed on the launcher and the RF source. In areas where a data base or analytical tools are lacking (*e.g.*, in the folded-waveguide design), prudent projections of the performance parameters have been used. Critical areas where R&D is needed have also been identified.

4.5.1. Folded-Waveguide Launcher

The folded-waveguide antenna [45] is proposed as the basic wave-coupling unit for the FWCD system. Each launching unit consists of a TE_{101} rectangular cavity folded several times in the long transverse dimension, with the same field pattern polarized with respect to the folded path (shown in Fig. 4.5-1). Wave power is coupled to the plasma via openings in the front, while a shorting plate is located at the back end of the cavity to match the waveguide impedance at the aperture to the plasma surface impedance. The resonant field structure inside the waveguide ensures relatively low electric fields at the coupling aperture. Attractive features of this innovative launcher concept include: (1) high power-handling capability ($\sim$40 MW/m^2) which is $\sim$4 times that of loop antennas, (2) a radiated field pattern similar to that of a loop antenna, (3) a simple configuration that can be adapted to a variety of port sizes and shapes, and (4) a robust structure making it resistant to normal disruptive loads. Even though loop antennas almost exclusively have been used in ICRF fast-wave experiments to date, their complex configurations have always been perceived as a drawback in reactor applications [46]. As such, the folded-waveguide coupler appears to be an attractive substitute for loop antennas in future devices. In addition, the high FWCD frequency ($\sim$140 MHz) asso-

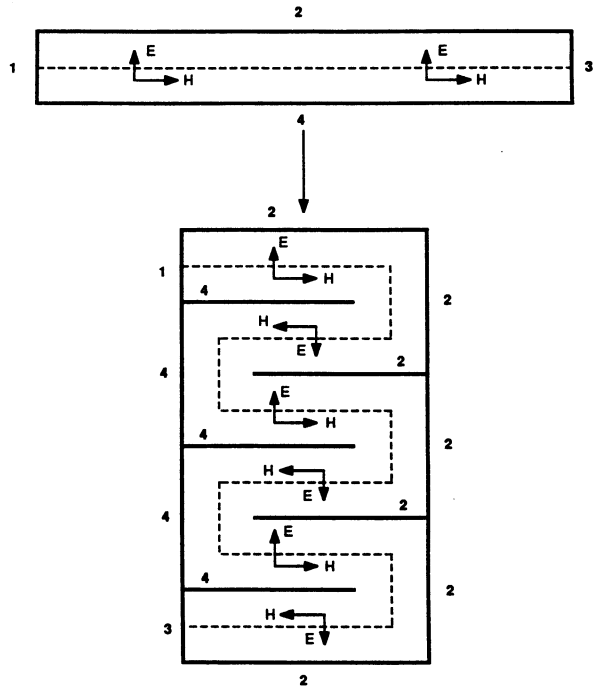

Figure 4.5-1. Normal-(unfolded-) and folded-waveguide cross sections and field polarizations.

ciated with the high magnetic field (~11 T) in ARIES-I further reduces the size of the waveguide and provides a unique environment for exploiting the favorable features of the folded waveguide.

Extensive low-power bench tests [47, 48] of the folded-waveguide concept were carried out at the Radio-Frequency Test Facility (RFTF) at Oak Ridge National Laboratory (ORNL). Both scaled-down and 80-MHz full-size versions of the waveguide were tested. Power was fed in with a coaxial line tapping the central member of the vanes separating the folds. With the waveguide coupled to free space, the field patterns both inside the cavity and outside the aperture were measured by magnetic probes and shown to agree well with theory. The most important result was that the measured field decay in the radial direction in front of the waveguide exhibited characteristics similar to those from a loop antenna of roughly the same size. Fast waves, therefore, can be launched easily from these structures.

Recently a series of high-power tests were performed on the 80-MHz waveguide at the same facility [49, 50]. All measurements were made in either vacuum or air. Some of the key results include:

- Pulse mode operation with 25-ms, 30-kW pulses and with a 5% duty cycle was achieved, with a maximum calculated electric-field strength, $E_{max} = 17$ kV/cm, inside the cavity. The test was limited to one second because of structure heating.
- A record $E_{max} = 43$ kV/cm has been reached with low duty-cycle pulses at a power level of 200 kW [51].
- Typical electric fields inside the cavity are about half of those for a loop antenna transmitting the same power, implying that the power handling capability of the folded waveguide can be four times that of the loop. In addition, typical values of the parasitic electrostatic fields at the waveguide mouth, which are perceived to be responsible for impurity generation, are weaker by a factor of 40 when compared to loops under the same conditions. Further experiments are planned to verify this claim.
- Multipactor breakdown, perceived to be an issue because of the large surface area inside the guide, was controlled successfully with prolonged baking by external heaters (*e.g.,* at 150 °C for three days) with subsequent RF conditioning.

The general conclusion from these experiments is that the high-power potential for the folded-waveguide launcher has been confirmed.

A schematic of the folded-waveguide unit designed for 141-MHz operation in ARIES-I is displayed in Fig. 4.5-2, with its dimensions and projected performance parameters listed in Table 4.5-I. Each guide will have six folds, each with a vertical height of 10 cm. To a good approximation, the cavity radial thickness, t_g, is given by

$$t_g = \frac{0.5\,\lambda_o}{\sqrt{1-(\lambda_o/2L_g)^2}}, \tag{4.5-1}$$

where λ_o is the free-space wavelength and L_g is the transverse-folded path length. To accommodate the launcher in one of the ARIES-I blanket modules, t_g needs to be shortened. By choosing $L_g = 1.80$ m, which is far above the TE_{10} cutoff but slightly below the TE_{20} cutoff, one finds $t_g = 1.32$ m. Further reduction of t_g can be achieved by introducing a diaphragm structure inside the waveguide, as described in Sec. 4.5.2.

The toroidal width of the folded guide is set to a quarter-wavelength (0.3 m) of the dominant $N_{||}$ (= 1.77) wave component of the launched spectrum. To avoid destructive interference of the fields from adjacent folds in the poloidal direction, the front of the guide is covered with a conducting, polarizing plate (Fig. 4.5-2) that completely shields out the waveguide fields from the plasma in alternate folds. In the open area of the plate, Faraday shields, in the form of rows of conductor strips parallel to the magnetic field lines,

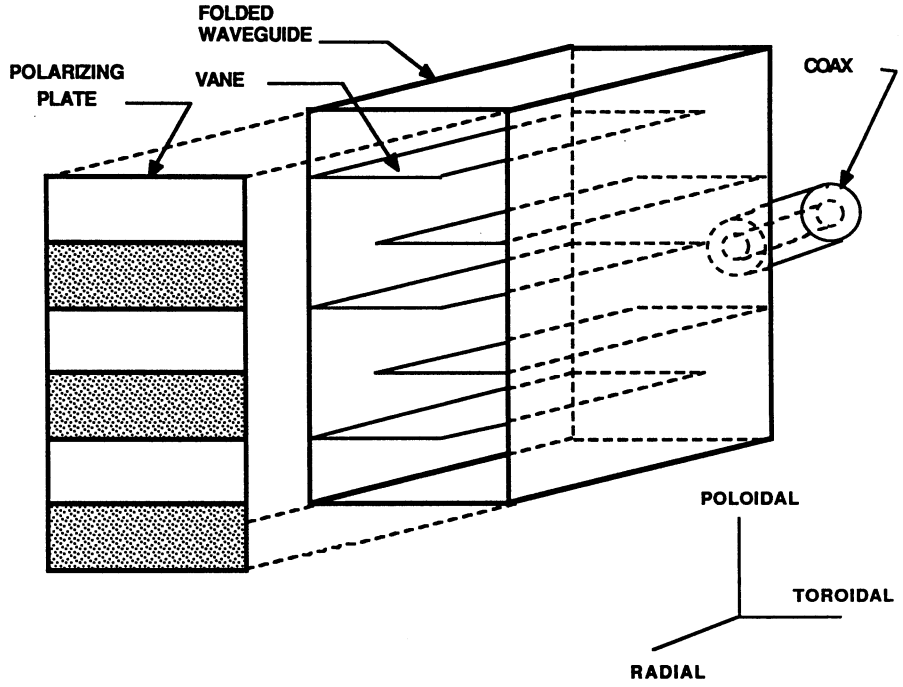

Figure 4.5-2. Isometric view of folded waveguide (without a diaphragm).

Table 4.5-I.
ARIES-I Folded-Waveguide Parameters

Number of folds	6
Unfolded-waveguide height (m)	0.10
Toroidal width (m)	0.30
Toroidal width of vane (m)	0.20
Poloidal height (m)	0.60
Unfolded-waveguide width (m)	1.80
Radial thickness (without a diaphragm) (m)	1.32
Radial thickness (with a diaphragm) (m)	0.80
Diaphragm thickness (m)	0.20
Diaphragm gap width (m)	0.04
Power transmitted (MW)	4.0
Coupling efficiency	0.99
Peak electric field (kV/cm)	25.0
Electric field at aperture (kV/cm)	1.34

are installed to short out the $E_{||}$ fields at the bends and to obtain optimal coupling to the fast-wave polarization. To isolate the synchrotron radiation from the cavity and the rest of the RF system, double rows of Faraday strips may be required. These metal strips should be shaped and arranged to minimize their transparency to the radiation while retaining their transparency to the RF waves. At the back plate, a tapered coax, which is 10 cm in diameter at the feedpoint (Fig. 4.5-1), is used to inductively couple the power into the waveguide. In principle, the locations of the back plate and the feedpoint, and the generator frequency can be adjusted to obtain a match between the plasma load and the feeding coax. The flat plates, or vanes, that separate the folds can be contoured to minimize the local electric field; in particular, the radii of curvature of the vane tips near the bends should be expanded.

4.5.2. Special Launcher Design Features

The ARIES-I blanket structural material is chosen to be silicon-carbide (SiC) composite because of its low activation, low decay afterheat, high strength, and other favorable thermomechanical properties (Sec. 8). For similar reasons, it is proposed that the launcher for the FWCD be built of SiC composite coated with copper. Well-proven coating techniques such as plasma spraying or chemical vapor deposition (CVD) processes can be used. It is believed that the bonding between the metal and the composite surface will be strong enough to withstand both the shear and "peeling" forces exerted on the interface during disruptions. It should be noted, however, that a data base for this aspect of the Cu/SiC interface does not exist, and that future experiments should be carried out to qualify the above statement.

Usually a coating thickness of several skin depths is sufficient to form a perfect metal surface on the SiC-composite waveguide structure. The skin depth, δ, of a wave with frequency, f, is given by

$$\delta = \left(\frac{\rho}{\pi f \mu_o}\right)^{1/2} , \tag{4.5-2}$$

where the conductor resistivity, ρ, is sensitive to the purity of the metal. In the presence of a neutron flux, nickel is the main impurity in copper, and at a wall loading of 3 MW/m^2, typical of ARIES-I, the Ni concentration, Y_{Ni} (in wt %), accumulates at a rate of [52]

$$Y_{Ni} \simeq 0.67\, t_y , \tag{4.5-3}$$

where t_y is the number of years of exposure. At the first-wall operating temperature of 800 K, the Cu-Ni resistivity evolves as [52]

$$\rho_{Cu-Ni}(\Omega\text{-m}) \simeq 5.0 \times 10^{-8} + 1.25 \times 10^{-8}\, Y_{Ni} . \tag{4.5-4}$$

At the end of 10 years of operation, the skin depth for the irradiated copper will be 14 μm so the coating thickness can be set conservatively at 50 μm.

Assuming perfect bonding between the Cu coating and the SiC surface, an assessment is made of the forces exerted on a single folded-waveguide structure during a plasma disruption [53]. At a projected current-decay rate of 1 MA/ms and using typical ARIES-I parameters, the currents and forces induced on the various parts of the launcher are given in Table 4.5-II. In the case where there is no support for the waveguide except at the rear wall, the calculated shear stress is about 26.4 MPa, which is about 1/10

Table 4.5-II.
Disruption Forces on a Waveguide Launcher

	Top/Bottom	Sides/Front/Rear
Equivalent resistance (mΩ)	4.0	1.36
Current (A)	1500	4412
Force (kN)	11.7	34.4

of the ultimate tensile strength for SiC composites at the operating temperature. The stress can be greatly reduced by providing periodic support (in the form of a picture frame made of SiC composite) along the tops and bottoms of the waveguide launchers. Since the structure derives its strength primarily from its compact shape, the waveguide wall thickness will have minimal effect on its integrity under stress. The wall thickness, therefore, is determined solely by the cooling requirement and 0.5 cm appears to be a reasonable choice.

In order to fit the waveguide launchers into one of the ARIES-I blanket modules, the radial thickness of the waveguide must be reduced to 0.8 m. As discussed in Sec. 4.4.1, the designed thickness of a folded waveguide at $f = 141$ MHz is 1.32 m and further reduction is obviously required. This can be achieved, for example, by introducing into each waveguide a simple diaphragm structure of finite thickness [54] and made of Cu-coated SiC, as shown in Fig. 4.5-3. This diaphragm (or obstacle) is a transverse ridge placed midway along the waveguide axis. At this location, the vertical height of the guide is reduced from b to b', giving the diaphragm an aspect ratio of b'/b. The diaphragm then functions as a capacitive phase shifter that effectively reduces the waveguide axial wavelength.

Approximate design curves for the waveguide thickness, t_g, as a function of the diaphragm thickness, t_D, and aspect ratio, b'/b, are shown in Fig. 4.5-4 for the transverse dimensions given in Table 4.5-I. To achieve a t_g of 0.8 m, the required obstacle should be 0.2-m thick and 0.06-m high. A rough estimate, in which only the fundamental cavity mode is accounted for, indicates that the peak electric field is approximately doubled at the same stored wave energy because of the presence of the diaphragm. The higher field

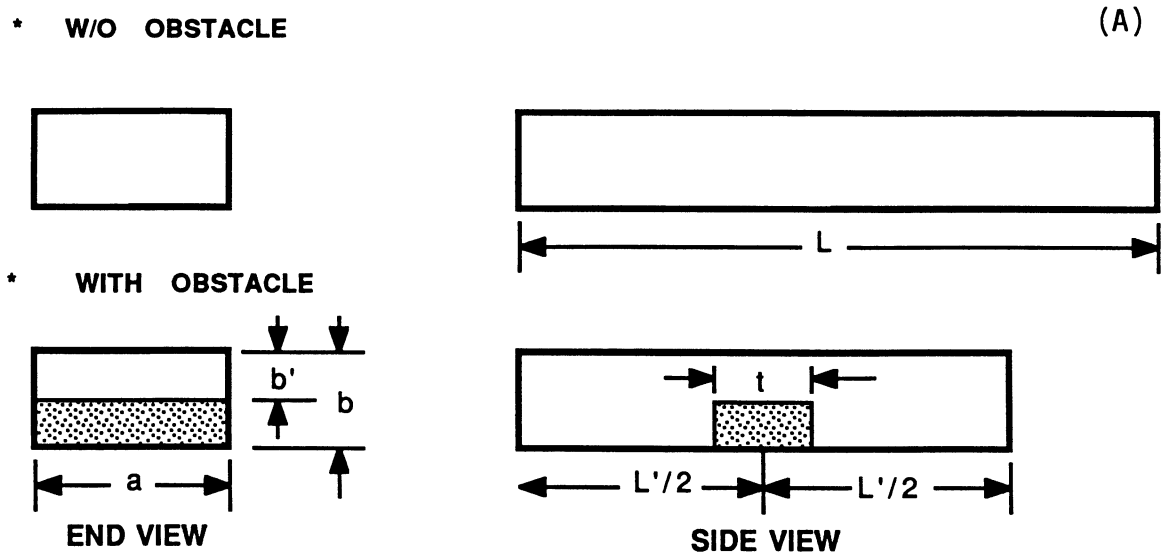

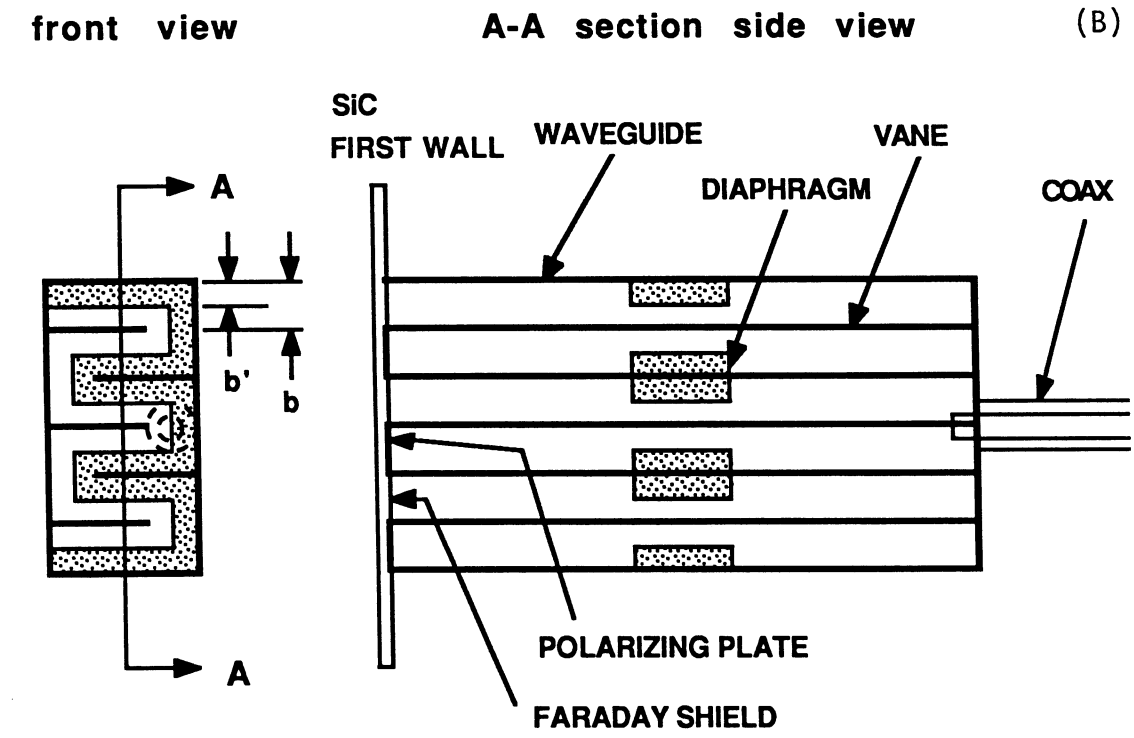

Figure 4.5-3. Front and side views of (A) an unfolded-waveguide cavity without and with diaphragm and (B) a folded-waveguide cavity with diaphragm.

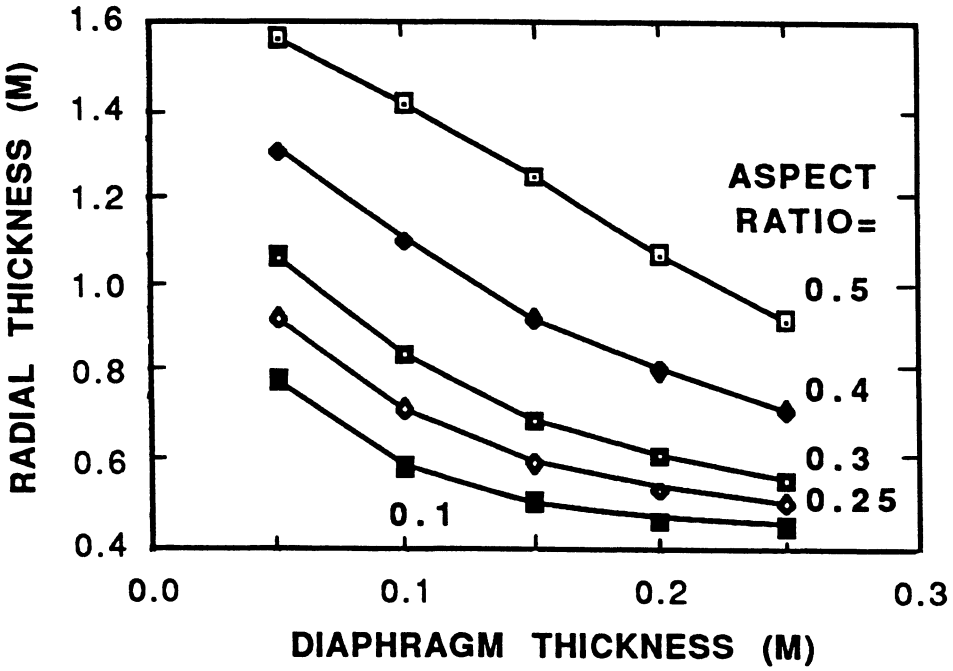

Figure 4.5-4. Radial thickness of waveguide unit as a function of diaphragm thickness.

may lead to increased wall dissipation of the wave energy, which potentially can cause local hot spots. However, in principle, this problem can be greatly alleviated by contouring the shape of the obstacle to reduce the local electric-field strength in a manner analogous to increasing the radii of curvature of the vane tips. It is evident from the cavity mode structure that peak dissipation occurs at the front and back ends and at the side walls midway along the waveguide axis. To cool the structure, horizontal tubes, using pressurized helium-gas coolant, can be placed near the ends without affecting the waveguide performance, while the diaphragm in the middle can provide space for coolant flow and extra support for the vanes, if desired. It should be noted that, while the appropriate design tools are being developed, a detailed picture of waveguide wall dissipation in the presence of a diaphragm, and the corresponding cooling requirements, is presently out of reach. Nevertheless, it is felt that as long as the dissipated power is kept to a few percent of the coupled power (*i.e.*, ~200 kW per guide), the required cooling should be manageable.

4.5.3. High-Performance Launcher Option

Making use of the special properties of the SiC composite, a further enhancement of the launcher power-handling capability may be possible, but it is not a necessity for

ARIES-I. The electrical properties of a ceramic material like SiC can be characterized by the complex relative permittivity, $\epsilon = \epsilon' - j\epsilon''$, where ϵ' is the relative dielectric constant having a range of 6.7–10.0, depending on the frequency [55]. The imaginary part of ϵ consists of two components: $\epsilon'' = (\sigma/\omega\epsilon_o) + \chi''(\omega)$ [56], which represents dissipation in the medium. The first component is due to conduction of free charges, such as electrons, ions, and holes, and is characterized by σ, the dc electrical conductivity. The value of σ depends on the atomic structure of the material and, for composites, can be tailored to a wide range of values by doping the material with conductor impurities. The α-SiC crystal conductivity ranges from 10^{-8} to 10^{6} mho/m, while the β-SiC crystal value of σ is reported to be between 0.1 and 10^{4} mho/m [55]. Introduction of elemental additives such as beryllium, boron, or aluminum produces the most pronounced effects [57]. For instance, SiC with added Be (1 wt %) showed an extremely low conductivity of about 3×10^{-12} mho/m, while SiC with added B or Aℓ had σ values of, respectively, 5×10^{-3} or 1.25×10^{2} mho/m. In general, ionizing radiation due to gamma rays tends to raise σ and is mainly a flux-dependent effect. On the other hand, neutron irradiation will produce microscopic defects that constitute phonon scattering sites, leading to a decrease in σ. Apparently temperature also has an effect on the value of σ during ionizing radiation, but the data in this area are still evolving. Nevertheless, it is clear that the electrical conductivity of SiC can be tailored to desired values.

The second component of ϵ'', $\chi''(\omega)$, is the imaginary part of the electric susceptibility of the material and is highly frequency dependent. This wave absorption mechanism arises from polarization effects on the bound charges within the material [58]. Among these effects are electronic and atomic polarizations characterized by large restoring forces and small damping effects, leading to resonance absorption usually in and above the infrared regime. Other processes such as dipolar and interfacial polarizations involve large damping effects that result in relaxation-type absorption in the microwave range of frequencies. To a large extent, the exact spectral locations of these absorption phenomena depend on the atomic and molecular structure of the material. For example, SiC is not a dipolar material, but radiation-induced defects may create asymmetrical molecules that have permanent dipoles so the associated relaxation absorption cannot be overlooked.

An extensive literature search reveals that for most non-irradiated ceramics, the loss tangent, $\tan\delta = \epsilon''/\epsilon'$, has measured values of 10^{-5} to 10^{-2} in the 1-MHz to 300-GHz frequency range [59]. On the other hand, data in the 1 to 3 THz range, corresponding to the synchrotron radiation spectrum for ARIES-I, are extremely rare. Data on the absorption spectra for SiC are virtually non-existent and must be inferred from similar data on common ceramics such as spinel and alumina [60]. Irradiation experiments on

these materials indicate that enhancement in $\tan\delta$ as large as several orders of magnitude is possible, but it can be controlled by careful tailoring of their composition.

At $f = 141$ MHz, the free-space wavelength of the fast wave is much larger than the wall thickness of the waveguide cavity ($\sim$0.5 cm). As an illustration, with $\epsilon' = 10$, the transmissivity of the wave through a 1-cm-thick SiC slab is found to be 99% just because of dielectric effects. To limit RF dissipation in the slab to less than 1% of the transmitted power, the loss tangent of the material has to be less than 0.125. This property should be easily satisfied for irradiated SiC with a careful selection of its composition, and the slab can be made transparent to the wave. The waveguide launcher can then be envisioned as a closed rectangular box made of thin (< 1 cm) SiC walls, with the polarizer and the Faraday shield in the front wall formed by the application of a copper coating of the appropriate pattern, as described in Sec. 4.5.2. The inside of the cavity can be pumped down to a high quality vacuum ($< 10^{-7}$ torr) which, together with its complete shielding from plasma particles and its well-conditioned inner surface, enhances the possibility that ultra-high electric fields ($\gg 50$ kV/cm) can be sustained without breakdown. As a point of reference, spark-over at 120 MHz was estimated to occur at a field level of approximately 120 kV/cm in vacuum without a plasma close by and without an ambient magnetic field [61]. There are, however, two main concerns: surface breakdown and vacuum integrity of the composite, neither of which has an adequate data base at present. Another concern is the integrity of the bonding between SiC and the Cu coating at high temperature operation, since Cu has a thermal coefficient of expansion four times that of SiC. This may be solved by embedding a fine copper-wire mesh inside the SiC wall, which essentially serves as a reflecting surface to the fast wave.

4.5.4. Wave Coupling Analysis

The coupling of the wave power from the individual waveguide to the plasma is investigated using the FWQ code [45]. This code approximates the fields inside the folded-waveguide cavity which is modeled as a narrow-height rectangular waveguide containing a series of inductive diaphragms at the front and a shorting plate at the back of the waveguide. The plasma is modeled as a semi-infinite medium, with a surface impedance, Z_p, that is separated from the waveguide mouth by a vacuum region of thickness, Δ. Approximating the form of the vacuum field, evaluating the cavity thickness, t_g, from Eq. (4.5-1), and applying the condition of power flux continuity at the waveguide mouth, the field pattern and its magnitude are completely determined in terms of the power coupled to the plasma, P_c. Another important quantity that is calculated by FWQ is

the coupling efficiency that is defined as

$$\eta_g \equiv \frac{P_c}{P_c + P_\Omega} \simeq \frac{Q_u}{Q_u + Q_\ell}, \tag{4.5-5}$$

where P_Ω is power lost to the walls of the coupler and Q_ℓ and Q_u are the quality factor of the cavity with and without plasma, respectively. Using the equivalent unfolded-coupler model and assuming that only the TE_{101} fields contribute to the wall losses, Q_u can be approximated by

$$Q_u \simeq \frac{\pi \eta_o}{4R_s} \cdot G, \tag{4.5-6}$$

where η_o (= 377 Ω) is the free-space intrinsic impedance, G is a geometric factor, and R_s is the cavity-wall surface resistance. The plasma-loaded quality factor, Q_ℓ, can be estimated from

$$Q_\ell \simeq \frac{\omega U_E}{P_c}, \tag{4.5-7}$$

where U_E is the energy stored in the wave electric fields of the system.

To calculate Z_p for ARIES-I, the scrape-off-layer density profile must first be cast into a 1-D form [62]:

$$n(x) = \begin{cases} \frac{2n_o}{a}\, x = \bar{n}\, \frac{x}{x_o} & x > x_o \\ \\ \bar{n} \exp\left(\frac{x - x_o}{x_o}\right) & x < x_o \end{cases}, \tag{4.5-8}$$

where x is the inward radial direction, a is the minor radius, n_o is the peak density, $\bar{n} = 2n_o x_o/a$, and

$$x_o = \left(\frac{a\, c^2\, \Omega_i^2}{2\, \omega_{pio}^2\, \omega^2}\right)^{1/3}, \tag{4.5-9}$$

with Ω_i and ω_{pio} being, respectively, the ion cyclotron and peak plasma frequencies.

As shown in Fig. 4.5-5, the scrape-off layer in ARIES-I is 0.1-m wide and has a high density and a relatively large density gradient, typically with $n_e = 8.7 \times 10^{19}$ m^{-3} at the separatrix and 2.5×10^{18} m^{-3} at the first wall. Thus, the coupling of fast waves to the plasma is dominated by the separatrix region of the scrape-off-layer density profile. An equivalent plasma radius, a', is used in Eq. (4.5-8) by setting $2n_o/a' = dn/dx$ at a representative point near the separatrix. After several tries, a value of $dn/dx \simeq 1.50 \times 10^{21}$ m^{-4}

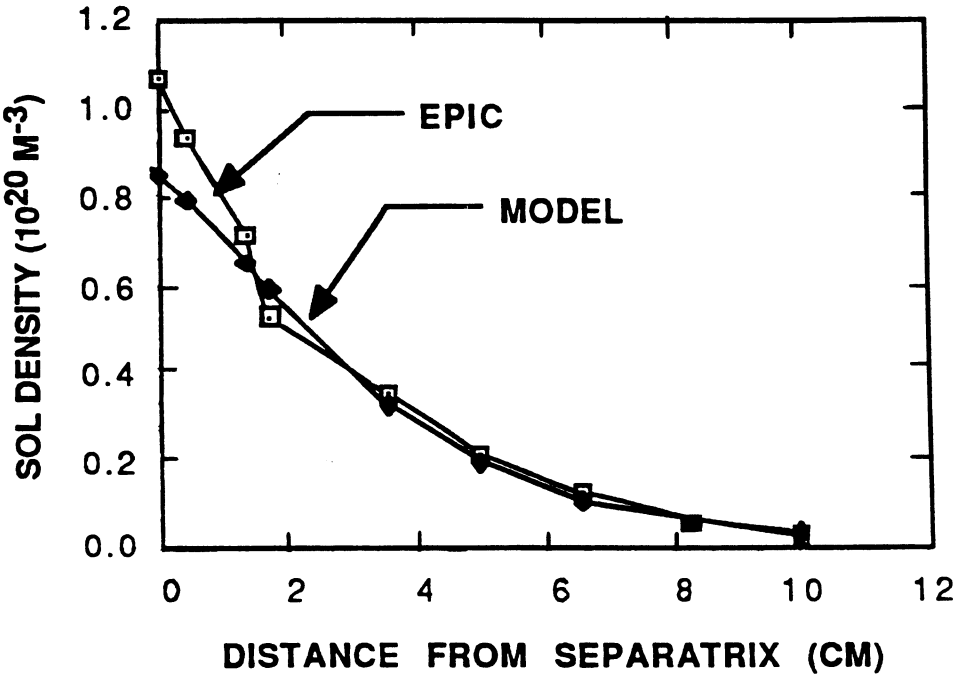

Figure 4.5-5. ARIES-I scrape-off-layer density profile calculated by the EPIC code (open squares) and the model density profile used in waveguide coupling calculations (open circles).

is chosen, with $a' = 0.25$ m, $x_o = 0.027$ m, and $\bar{n} = 4.12 \times 10^{19}$ m^{-3}. This model density profile, as characterized by Eq. (4.5-8) and displayed in Fig. 4.5-5, appears to be a reasonable fit to the calculated profile. With fast-wave wavelengths that are long compared to x_o, the plasma surface impedance Z_p at $x = x_s$ is given by [62]

$$Z_p(x_s) = 3.117\,\omega\,\mu_o\,x_o\,, \tag{4.5-10}$$

with x_s defined as the radial location where $E_{||} = 0$ and $n(x_s) = 0.3\bar{n}$. Knowing $\bar{n}$ and the scrape-off-layer density profile, the location x_s is found to be -0.005 m or, equivalently, the distance between the plasma surface and the waveguide mouth ($\Delta = 0.039$ m). Using these parameters as inputs to the FWQ code yields the following results: $Z_p = 98.5\ \Omega$, $\eta_g = 0.99$, $E_{peak} = 25.0$ kV/cm, and $E_{aperture} = 1.34$ kV/cm for a coupled fast-wave power of $P_c = 4.0$ MW (Table 4.5-I). The value of the peak electric field (25 keV/cm) is considered modest in comparison to the maximum standoff field already achieved in high-power ICRF heating experiments (~40–50 kV/cm). The low electric field at the waveguide aperture and the large distance of the peak field location from the plasma surface (~0.4 m, with diaphragm) makes this launcher system less susceptible to impurity generation.

This problem may also be mitigated by the launching of a unidirectional wave spectrum peaked at a finite $N_{||}$, as in ARIES-I. To couple a waveguide array to a unidirectional wave spectrum, some modification to the above results is in order and will be discussed in Sec. 4.5.5.

4.5.5. Phased-Array Launcher Design

Toroidal phased arrays of the folded-waveguide units are required to generate a current profile with FWCD power which, together with the inherently driven bootstrap current, forms the equilibrium current profile. The overall launching system consists of two poloidally stacked waveguide modules located above the equatorial plane on the outboard side. The configuration is shown in Fig. 4.5-6 and the operating parameters are listed in Table 4.5-III. Note that the nominal power flux of $\sim$40 MW/m^2 through the waveguide aperture is four times the maximum achievable value of $\sim$10 MW/m^2 for loop antennas.

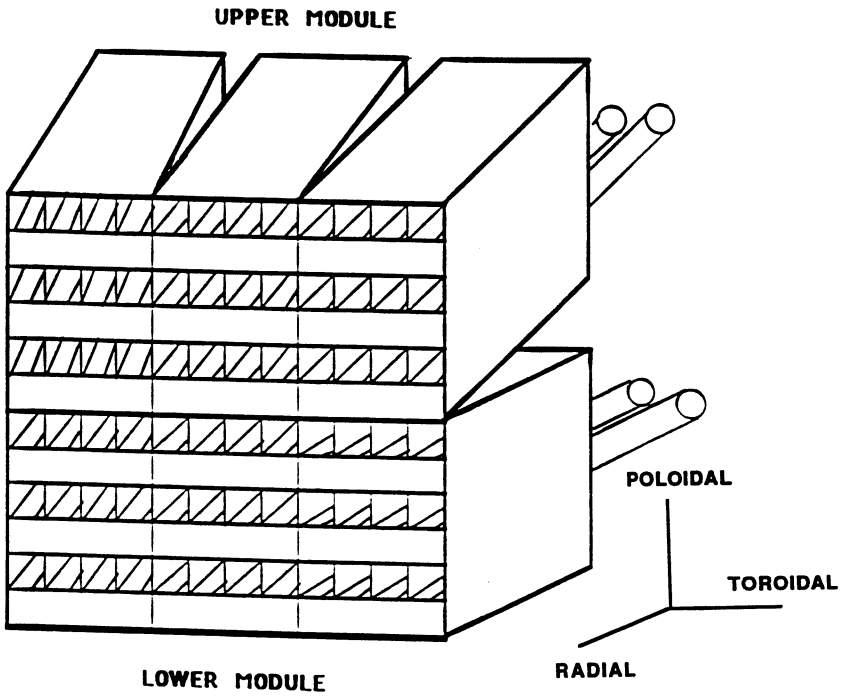

Figure 4.5-6. Isometric view of two poloidally stacked, 12-waveguide modules for current drive and profile control on ARIES-I.

In order to launch the desired unidirectional wave spectrum centered at $N_{||} = 1.77$, each module comprises a toroidal array of 12 waveguides, each of which is fed by a coax with a 90° phase shift between adjacent units. Each module will then have a toroidal width of 4.25 m × 0.7 m, including the 0.5-cm-thick waveguide walls. The overall coupling system occupies approximately 0.96% of the total first-wall area. Simulations with a 2-D magnetostatic loop-antenna code, CAV2D [63], indicate that a maximum directivity of 0.95 is possible with such a module. The corresponding power spectrum evaluated

Table 4.5-III.
Design Parameters of FWCD Launcher System

Per module	
Number of folded waveguides	12
Wall thickness (cm)	0.5
Toroidal width (m)	4.25
Poloidal height (m)	0.70
Radial thickness (m)	0.80
Relative phase shift (°)	90
Peak refractive index	1.77
Directivity	0.95
Coupling efficiency	0.97
Power delivered (MW)	48
Overall system	
Number of modules	2
Poloidal locations of modules (°)	25, 46
Total power delivered (MW)	96
Total first-wall perforation (%)	0.96

at the plasma surface is displayed in Fig. 4.5-7. The finite poloidal extent of each module introduces a non-negligible spread in the poloidal wave-number spectrum that is symmetric around $N_\theta = 0$. By properly phasing the two launcher modules, a degree of directionality, which is required for current profile control, could be introduced into the poloidal wave spectrum, as outlined in Sec. 4.4.

The analytical tools for accurate evaluation of the coupling efficiency of the launcher modules have yet to be developed. However, a rough estimate of the coupling efficiency can be made by comparing the reflectivity of FWCD power from the plasma surface between incident spectra centered at $N_{||} = 0$ (single-waveguide case) and $N_{||} = 1.77$ (12-waveguide case). The reflectivity values are, respectively, 0.31 and 0.66. Thus, for the multiple-waveguide case, at least twice as much power is reflected back into each individual waveguide as with the single-waveguide case. This means that, for the same transmitted power, at least twice as much power is dissipated in the walls for the phased array. As indicated in Table 4.5-I, the coupling efficiency for a single guide is 99%; conservatively, in the ARIES-I design, the coupling efficiency for the launcher modules is taken to be 97%.

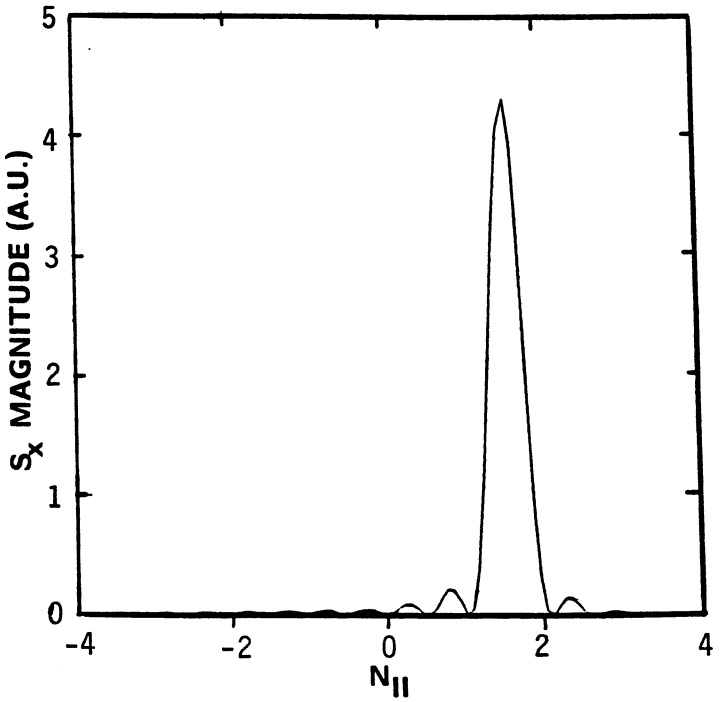

Figure 4.5-7. Power spectrum at the plasma surface from the 12-waveguide launcher module for ARIES-I, calculated by the CAV2D code [63].

4.5.6. Design and Performance of the RF System

The FWCD has a relatively modest efficiency ($\gamma \sim 0.35$) and, therefore, maximizing the overall electrical efficiency of the RF system becomes critical in order to minimize the amount of recirculating electric power in the reactor. Primarily because of the low frequency that is used, it is anticipated that this system will utilize mostly "off-the-shelf" technology, and only a modest development program will be required to upgrade the performance parameters of its key components to the desired levels. Unit costs of the RF system are significantly lower because the number of sources is reduced. Thus, emphasis of the design effort has been focused on the development of a high-efficiency (~90%), high-unit-power (~5 MW) RF source. As for the rest of the system (*i.e.*, transmission line, phase-shift and matching circuits, and waveguide feeds), only a brief description will be given together with an estimate of their efficiencies.

The designated frequency range of operation for the RF current drive and heating system is 140–175 MHz, which is out of the realm of efficient operation of the conventional tetrode because of excessive screen dissipation at higher frequencies ($P_{sc} \propto f^{2.5}$) [64]. As an alternative, other tubes were considered. Among them, the klystrode [65], the Resnatron [66], and an improved tetrode [68] were identified as viable options. The first two devices were invented several decades ago with the first prototypes exhibiting impressive parameters. At 450 MHz, the klystrode, then known as the inductive output tube, gave a 100-W continuous-wave (CW) output at 35% efficiency and a 10-dB power gain. For the Resnatron, a 50- to 80-kW CW output power at 412 MHz with a 79% efficiency was recorded. Development of both of these tubes was subsequently stopped because of a lack of commercial interest. In the early 1980s, interest in the klystrode was revived [67], based on its promise as an efficient, high-power (sub-MW) transmitting tube for UHF television stations. Since then, the EIMAC Division of Varian Associates has developed these tubes, with parameters ranging from 60-kW CW power with 65% efficiency (for commercial markets) to 0.5–1.0-MW CW power at 425 MHz and with ~75% efficiency and ~23-dB gain (targeted for defense applications) [68]. Significant advances have also been made in tetrodes. Recent tests of the Varian EIMAC X2242 tetrode in the JT-60 ICRF system [64] recorded a CW output power of 1.5 MW at 110 MHz and 1.6 MW at 131 MHz. An upgraded version of this tube, the X2274 tetrode, capable of 1-MW CW output at 160 MHz and 65%–70% efficiency, is being developed for JT-60 and CIT applications [68]. Even though all three options are promising for high-efficiency power generation, the current-drive system for ARIES-I will use the klystrode as the reference source.

The klystrode is a linear beam device having the desirable features of both a klystron and a tetrode, in contrast to the radial beam Resnatron. In Fig. 4.5-8, the schematic of a klystrode tube [67] is displayed. The major limitation to the power output of a conventional tube has been the dissipation at the grid and at the anode. In a klystrode, non-intercepting electrodes are used with the help of a focusing magnetic field deployed coaxially with the electron stream emitted from the cathode. The grid, made from pyrolytic graphite for thermomechanical stability [64], is placed ~1 mm from the cathode for optimal beam performance. The resulting bunched or density-modulated electron beam is then accelerated through the apertured anode at high potential without interception. It continues through a field-free region where the kinetic energy of the electrons is converted, via an output gap, to electromagnetic energy in the resonant cavity. The spent beam then passes through a second field-free region, the tailpipe, with minimal interception before it reaches the collector.

The best performance achieved to date on a klystrode tube is 0.5–1.0 MW at ~75% efficiency and ~23-dB gain. Improvements to this performance, in terms of better efficiency and higher power output per tube, can be made. Beam-induced surface currents in the output cavity constitute a power sink, which may be mitigated in the future with the use of high-temperature superconducting materials for the cavity structure. The

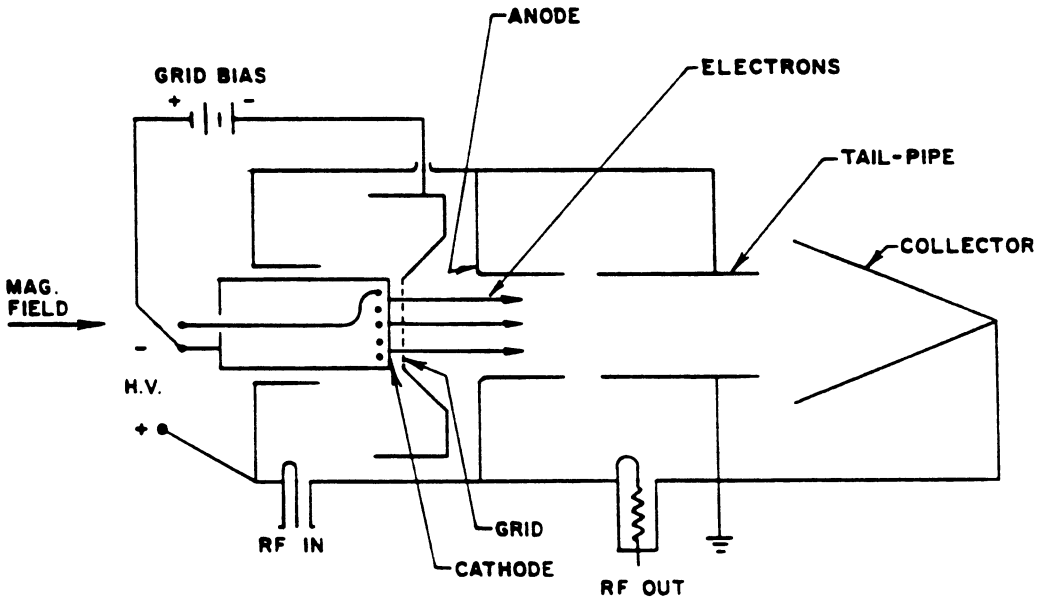

Figure 4.5-8. Schematic of a klystrode tube assembly [67].

field-free regions in the tube configuration ensure that the output interaction space is isolated from the input grid-anode space and also from the collector. Thus, the collector can be made very large to intercept the spent beam at low-power density. The idea of multistage depressed collectors, where the collector potential is reduced to below that of the tube body, can also be included in the design to recover the kinetic energy of the spent beam in the form of potential electric energy that would otherwise be converted into heat upon impact. Backstreaming of electrons to the cathode region as a result of collector depression can be minimized by designing the collector to function as a secondary electron trap. Coating the collector surface with a substance such as titanium, which has a low secondary-emission coefficient, would accomplish this purpose.

Since the tube structure between anode and collector resembles a klystron, the output power scales as $P \propto f^{-2.5}$ for constant efficiency, thus favoring low frequency operation. The optimum beam diameter should be proportional to $1/f$, which, for low frequency operation, implies larger cathode diameter, lower current density (particularly at higher energy), and longer tube lifetime. The lower frequency limit of these tubes is set by the physical size of the circuits involved, especially the output resonant cavity. More sophisticated cavity designs that provide smaller size and good bandwidth are feasible. Ultimately, the maximum CW power output at the frequency range of operation for ARIES-I is limited by the maximum beam voltage which is, in turn, determined by practical considerations such as cost and size rather than by electronic factors such as high-voltage breakdown in the tube. For the klystrode, a target performance of 5 MW per tube would require methods to increase the beam perveance, which would add complexity to the device. In this regard, the inherent low-voltage (30–60 kV) operation of the tetrode and the Resnatron make them very attractive.

It should be noted that all of the proposed improvements on the klystrode assembly involve extrapolations from present-day technology. Similar arguments can be made about the tetrode and the Resnatron. With a reasonable R&D effort, a prudent projection is that 5-MW, 90%-efficient tubes at a unit cost of \$1/W should be achievable within the 20- to 30-year time frame of ARIES-I construction [68].

Each of the 24 waveguide-launcher units is fed with a coaxial transmission line that transports 4–5 MW of power from a klystrode tube through the shield section. The line is envisaged to be a standard 20-cm-diameter, 30-Ω copper coax cooled with pressurized helium in the center conductor. A matching system will consist of a stub tuner and a line stretcher, while phase shifts between waveguides can be achieved electronically at low power. The distance between the matching system and the launcher feedpoint should be small in order to minimize power dissipation in the unmatched section of the line

where the voltage standing-wave ratio exceeds unity. The voltage limit in this section is often determined by the ceramic spacers that hold the central conductors in place. Careful choice of the spacer material and shaping of the spacers and conductor surfaces will help maximize this voltage limit [46]. A vacuum window should be placed at the point where the coax goes behind the shield. Beyond this point, the line should be pressurized with an inert gas such as dry nitrogen ($\leq$ 4 bar) or evacuated to raise the voltage standoff, particularly in the unmatched section. This section of the line may be coated with silver (or superconducting material) to further minimize wall dissipation. The entire transmission system is first matched at full power operation. Subsequently, minor excursions in the plasma loading can be tuned out by low-power electronic control of the phase shifters and by small adjustments of the frequency of the whole system. Experience with precise control of the phase shifts among a large number of adjacent antennas or waveguides is virtually nonexistent. Even with the mutual coupling among the various launcher elements [69], the task is perceived to be achievable with more design and operational experience in the coming years.

Near the feedpoint to the waveguide cavity, the coax should be smoothly tapered ($\sim$10 cm in diameter) in order to fit into the center bend at the backplate (Fig. 4.5-2). The center conductor should be closed and extended to form a loop with the center vane tip, thus magnetically coupling the wave energy to the waveguide. The detailed design of the feed geometry is quite challenging and is beyond the scope of this work.

As indicated in Table 4.5-IV, the maximum projected RF-system electrical efficiency, from wall plug to plasma, is estimated to be 71%, taking into account the fast-wave launcher directivity.

4.5.7. Critical Issues

To date, all of the experimental data on the folded-waveguide coupler have been collected from a test stand in the RFTF facility at ORNL. Field measurements were made when the waveguide was coupled either to free space or to an absorptive sheet placed some distance from the aperture. As noted in Sec. 4.5.1, the high-power capability of this launcher in terms of a high-voltage standoff has already been demonstrated. The most critical issue is to verify similar high-power properties of the waveguide in the presence of a plasma in a tokamak device. In this regard, a series of tests could be carried out, progressing from a low-power, single-waveguide coupling demonstration to high-power, current-drive experiments with a phased-array launcher.

Table 4.5-IV.
Projected RF-System Efficiency

Power supply (dc)	0.95
Transmitter (klystrode)	0.90
Transmission line, and phase-shift & matching circuits	0.90
Launcher coupling efficiency	0.97
Launcher directivity	0.95
Overall electrical efficiency	**0.71**

In conjunction with the experiments, there is a need to develop an advanced modeling tool for the waveguide coupler that could be used to analyze experimental data and project performance in a reactor plasma. In the case of ARIES-I, this analytical tool should have the added capacity to model a toroidal array of waveguide units. The useful design parameters that can be obtained from this code are the peak electric field in the RF launcher system and the coupling efficiency. Because of the complicated geometry involved, this tool is most likely going to be a 3-D finite-element electromagnetic code.

There are a few critical engineering issues related to the ARIES-I folded waveguide that need special attention. They are: (1) fabricating the waveguide structure with SiC composite, (2) cooling the waveguide structure, (3) reducing its radial thickness (or length) by using diaphragms, (4) contouring the vane tips and diaphragms to reduce local peak fields, and (5) optimizing the coax-feed location and detailed geometry. To design for the high-performance launcher, electrical properties of SiC composites in the ion-cyclotron-to-infrared range of frequencies and under a neutron fluence, including data on RF surface breakdown, should be studied and documented. With regard to the RF support system, demand for technological extrapolation appears to be moderate. Upgrading the efficiency (to 90%) and power output (to 5 MW) of tubes such as klystrodes, Resnatrons, and tetrodes is a crucial development issue that needs to be addressed. Likewise, to accommodate a varying plasma load, the appropriate matching and phase-shift circuits for high-power applications need to be developed.

4.6. NEUTRAL-BEAM CURRENT DRIVE

As stated in Sec. 4.2, fast-wave current drive (FWCD) is determined to be the primary scenario of steady-state operation in ARIES-I, with neutral-beam current drive (NBCD) chosen as an alternative. The NBCD offers several attractive features, among which are a potentially high current-drive efficiency ($\gamma \sim 0.5$–0.6) and a maturing experimental data base. It is considered, therefore, the most appropriate current-drive scenario for a near-term device such as ITER, where the demand for technological advances appears manageable and reactor engineering compatibility is not of critical concern. Nevertheless, it is of interest to explore the potential of implementing this current-drive technique in the ARIES-I environment, as a companion study to FWCD. In this section, the physics modeling of NBCD is reviewed and an operating scenario for ARIES-I is determined. A brief description of a neutral beam injection (NBI) system based on the RF quadrupole accelerator is also presented, together with a list of mainly technological issues that need to be resolved.

4.6.1. Physics and Base Scenario

An alternative current-drive scenario using negative-ion-based, high-energy neutral beams has been considered for ARIES-I. There is a growing experimental data base from various devices that documents current drive in the plasma by neutral beams. In the DIII-D tokamak, the plasma current was sustained by NBIs alone in H-mode-quality, high poloidal-beta discharges [16], while experiments on TFTR [6] and JET [7] indicated that NBCD can provide the required seed current for the bootstrap effect. The results from these experiments are in good agreement with theoretical predictions.

Because of its developing data base, credible physics, reasonable projected current-drive efficiency, compatibility with H-mode operation, and capability for detailed profile control, NBCD has been considered the leading option for steady-state operation in next-generation tokamaks such as ITER. However, in reactor applications, neutral beams in excess of 2 MeV will be required for core current drive, implying significant extrapolations from present-day technologies.

The first step in calculating the current profile and the associated current-drive efficiency by NBI is to determine the rate of fast-ion deposition in the plasma. In the computations performed for ARIES-I, this is accomplished by using the Monte Carlo code, NFREYA [70, 71]. The code calculates the beam deposition profile, $H(\psi)$, as a function of the poloidal flux, ψ, on 2-D flux-surface geometry generated by the free-boundary

MHD code, NEQ [72] to ensure consistency with the reference ARIES-I equilibrium. The fast-ion deposition rate is

$$\dot{n}_f = \frac{H(\psi)\,\Delta^3\psi\,I_b}{V_p}, \tag{4.6-1}$$

where I_b is the equivalent atomic current of the beam, V_p is the plasma volume, and $\Delta^3\psi$ is the volume between the flux surfaces ψ and $\psi + \Delta\psi$. The divergence, focusing, and shape of the neutral beamline are taken into account in the determination of $H(\psi)$.

The fast-ion deposition is determined by the atomic processes involved in the effective ionization of the NBI atoms. At the high beam energies and for plasma densities that are typical of ARIES-I, multistep ionization effects become important. In these calculations, the effective beam-stopping cross section has been evaluated, using an analytic fit based on recent computational results that allow for multistep ionization of the beam in collisions with the plasma constituents and impurities [73, 74]. The atomic data base needed for these calculations has been documented using the best data available [74].

The flux-surface-averaged current density due to the fast ions, $\langle j_{f\|} B\rangle$, is calculated from the uniform-field solution to the Fokker-Planck equation for the fast ions [75]. This fast-ion current is partially cancelled by the electron return current induced by the drag of the plasma electrons on the fast ions. It is modified, in turn, by neoclassical electron-trapping effects. The net flux-surface-averaged current density, driven by the neutral beams, is then

$$\langle j_{\|}^{NB} B\rangle = \left\{1 - \frac{Z_b}{Z_{eff}}\left[1 - G(Z_{eff}, \epsilon)\right]\right\} \langle j_{f\|} B\rangle , \tag{4.6-2}$$

where Z_b is the atomic number of the beam ions, and G is the trapped-electron correction factor which has been calculated by Start and Cordey [76] for all aspect ratios and is approximated here by a parametric fit [77].

Using the formalism described above, a series of calculations has been carried out to determine the required NBCD power for the reference ARIES-I parameters. Criteria for the selection of beam energy and other design parameters of the NBCD system (injection angles, focal lengths, *etc.*) include adequate current generation at the magnetic axis, high current-drive efficiency, and minimum shine-through. Since the purpose of the neutral beams is to drive the required seed current, the NBCD parameters (beam energy, E_b, and beamline aiming) are varied until the NBCD-driven current matches the required seed-current profile. The flux-surface-averaged seed current is calculated [28] as the difference

between the parallel current required from equilibrium, $\langle j_{||} B \rangle / \langle B^2 \rangle$, and the bootstrap current, $\langle j_{||}^{NC} B \rangle / \langle B^2 \rangle$.

It was found that the required seed current in the ARIES-I reactor can be driven with two beamlines at different injection angles. The first one, with beam energy $E_b = 3$ MeV and a tangency radius $R_{tan} = 7.3$ m, is aimed inside the magnetic axis in order to peak the current density profile at the center. The second beamline, with beam energy $E_b = 2.5$ MeV and a tangency radius $R_{tan} = 7.9$ m, is aimed outside the axis for broadening the current density profile. Both beamlines are aligned parallel to the equatorial plane of the reactor. Modeling of the beamline geometry is based on the Oak Ridge National Laboratory (ORNL) design and will be described in Sec. 4.6.2.

The results of the calculations are shown in Figs. 4.6-1 and 4.6-2, and reasonable agreement is obtained between the NBCD-driven and target seed-current profiles. The current-drive efficiency, η_{NB}, for this system is equal to 0.053 A/W, leading to a figure of merit of $\gamma = 0.52$. For a 68% bootstrap-current fraction, about 60 MW of NBCD power would be needed to drive the required seed current. The shine-through from both beamlines is less than 0.3%.

4.6.2. Neutral Beam System

In the previous section it was determined that beam energies on the order of 2–3 MeV will be necessary to drive the required seed current with an acceptable current-drive efficiency in the high density environment of ARIES-I. These energies are at least an order of magnitude higher than are typically found in existing NBI heating systems. Considering the formidable design limits that electrostatic-quadrupole (ESQ) beam-accelerator systems would face at these high energies, an NBCD system using RF quadrupole (RFQ) accelerators appears to be the choice for ARIES-I [78, 79]. These accelerators have been operated successfully in many research centers in the U.S. and other countries, and a large experimental data base already exists, albeit at much lower current ranges and pulse lengths than those required for fusion applications. Calculated energy efficiencies from conceptual designs of RFQs, with output currents > 1.0 A, exceed 75% at room temperature. Potentially, these efficiencies can be raised to 81% with further design improvements, leading to an overall wall-plug-to-ion efficiency of about 60% [78].

The NBCD system considered for the ARIES-I study is based on a design concept developed at ORNL [78]. A schematic of this design is shown in Fig. 4.6-3. Each beamline module consists of two vertical columns of beamlets. Assuming that each RFQ delivers

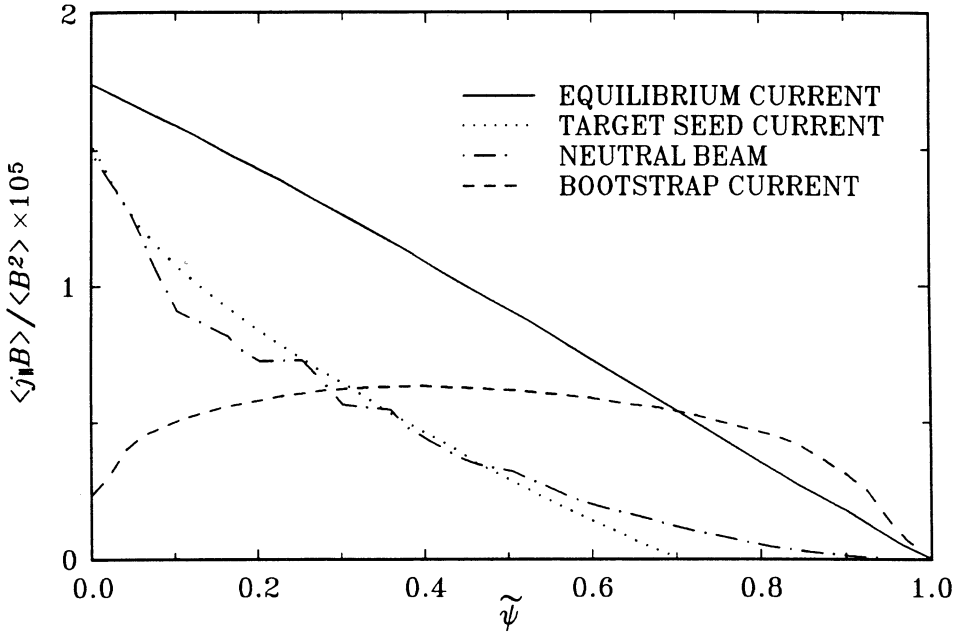

Figure 4.6-1. Contributions to the flux-surface-averaged current drive from NBCD and bootstrap effect (H).

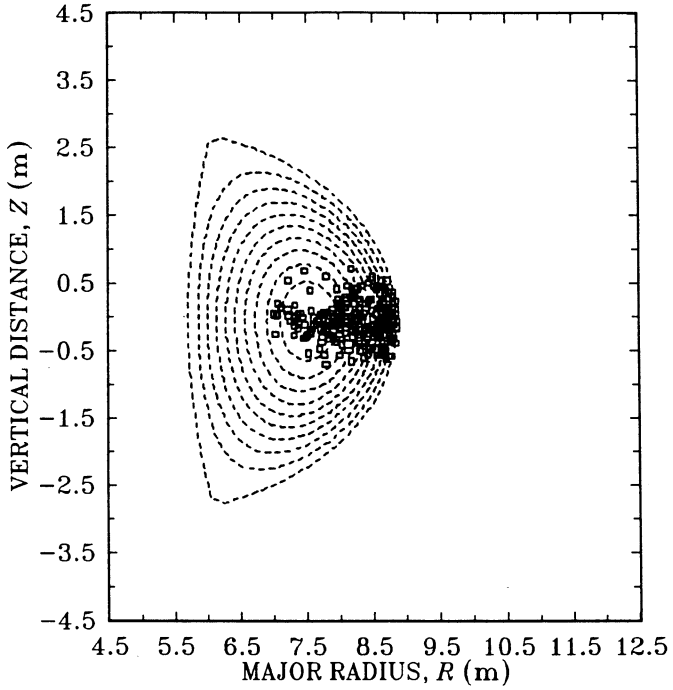

Figure 4.6-2. Deposition of fast beam ions in the plasma cross section from the two beamlines.

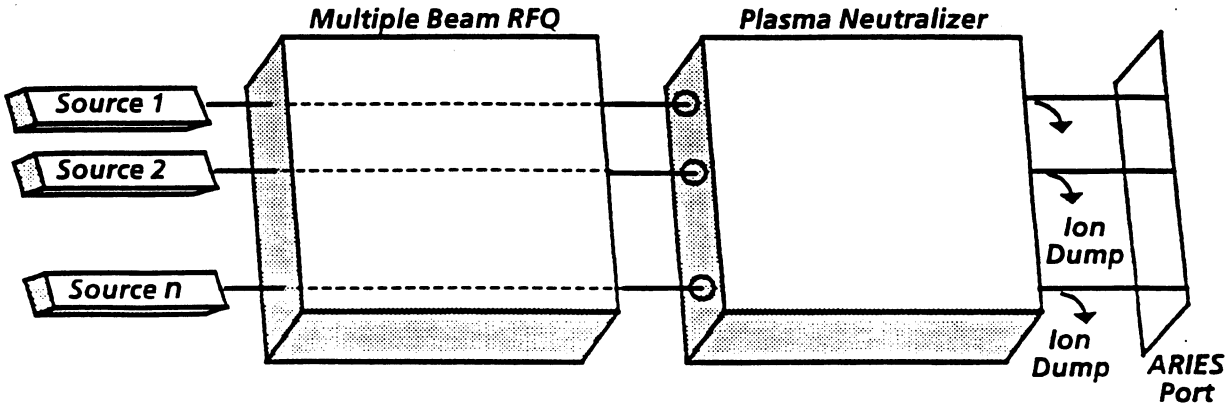

Figure 4.6-3. Schematic of the ARIES-I NBCD system [79].

0.5 A of output current, a minimum of 2×11 beamlets for the 3-MeV module (2×12 beamlets for the 2.5-MeV module) will be required to provide the 60 MW needed for current drive. The beam divergence of the 40-MHz RFQs is expected to be about 10 mrad and the required port size would be 0.85-m wide and 4.0-m high.

The other major components of the RFQ-based NBCD system for ARIES-I are the negative ion source, the low-energy-beam transport system, the neutralizer, and the beam dump. Because of the low efficiency of gas neutralizers, either a plasma neutralizer (efficiency ~80%–85%) or a laser neutralizer (efficiency > 95%) using photodetachment techniques to convert negative ions to neutrals should be considered.

4.6.3. Critical Issues

There is a growing experimental data base for NBCD and relatively good agreement between theory and experimental results exists. Degradation of the current-drive efficiency due to short-wavelength Alfvén instabilities has been shown not to be a major problem [80], while results of recent calculations [74] have greatly enhanced confidence in NBI penetration to the reactor plasma core. Plasma rotation as a result of unbalanced,

tangential neutral-beam injection may adversely affect the current-drive efficiency in present-day experiments. But in a reactor like ARIES-I, this would not be a concern because of the small momentum per ion deposited by the multi-MeV neutral beams [81, 82].

The technological problems associated with the design of an NBCD system for ARIES-I appear to be quite challenging when compared to the FWCD RF system. Although rapid progress has been made in RFQ technology, two critical issues remain to be addressed: scaling up the pulse length from milliseconds to continuous operation, and upgrading the current capability from 10s to 100s of mAs [78]. Similarly, while present-day negative-ion sources already have the current density and gas efficiency required for ARIES-I application, their pulse lengths need to be extended to CW operation [78]. Substantial development will also be required to produce efficient CW laser systems for use in photodetachment neutralizers [83]. To solve these difficult problems, an aggressive beam-development program needs to be undertaken in the next two decades so that the relevant technology can become available in the ARIES-I time frame.

4.7. SUMMARY

Steady-state operation of fusion reactors offer significant cost savings through: (1) improved performance of key reactor components, (2) higher availability because of more reliable performance, (3) a less expensive and smaller poloidal-field system due to the long start-up time (possible with current-drive assist), and (4) elimination of thermal power storage. These advantages should be balanced against the recirculating power fraction needed to maintain the plasma current. Three parameters affect the choice of the current-drive system: (1) the fraction of the equilibrium current provided by the bootstrap effect, f_{BS}; (2) the normalized efficiency of generating current within the plasma, $\gamma \equiv n_e I_p R / P_{CD}$; and (3) the electrical efficiency of the current-drive system including the efficiencies of the source, transmission, and power absorption in the plasma.

The approach used in ARIES-I is to increase the bootstrap-current fraction, f_{BS}, by operating at high poloidal beta by raising the on-axis safety factor, q_o, significantly above unity. The bootstrap fraction was estimated for a series of stable plasma equilibria using the best available transport coefficients. It is found that a value of $f_{BS} > 0.8$ is achievable with $q_o \simeq 2.1$. The penalty associated with a large safety factor is the reduction of the toroidal beta. Trade-offs between the bootstrap fraction and the beta values have led to the reference ARIES-I design with $f_{BS} = 0.68$ with $q_o \simeq 1.3$ and an extremely flat density profile. The bootstrap-current fraction can be increased drastically (up to 0.9) if a peaked density profile can be provided.

Among the current-drive options, the negative-ion neutral beam and fast waves in the ion-cyclotron range of frequencies were studied in detail. Both options are shown to perform well in terms of recirculating power. Neutral-beam current drive has a more developed experimental data base. However, fast waves have been chosen as the reference driver because of advantages in fusion-power-core engineering and integration, lower source unit cost, and a more mature source technology than multi-MeV negative-ion beam sources.

Significant improvements in the theory of fast-wave current drive were achieved during the course of the ARIES-I study by including the transit-time magnetic-pumping and electron-trapping effects. The wave frequency is set at 141 MHz, and the wave spectrum and the launcher position and phasing are chosen so that the sum of the driven and bootstrap currents matches the equilibrium current-density profile. The current-drive power is $\sim$90 MW, and the normalized efficiency is $\gamma = 0.31 \times 10^{20}$ A/W-m^2 in the absence of bootstrap. The current-drive power is also used for current ramp-up and for heating the plasma to ignition. Provision for a small amount of lower-hybrid current-drive power ($\sim$5 MW) is also made in the design for low density start-up and for current-density profile control in the plasma periphery.

As conceived for ARIES-I, the RF current-drive system primarily uses present-day technology, and only a modest development program is needed to upgrade the key components to their desired performance parameters. The RF source consists of klystrodes, which are presently used as UHF transmitters in television stations. Tetrodes and Resnatrons are also considered viable options. Folded waveguides are used as basic wave-launcher units, and are perceived to be superior to loop antennas for reactor applications because of their higher power-handling capability and more robust structure. The entire launching system comprises two poloidally stacked launcher modules, each consisting of a phased toroidal array of 12 waveguides. The launchers are located above the mid-plane on the outboard edge and occupy $\sim$0.96% of the reactor first-wall area. The wall-plug-to-plasma efficiency of the RF system, including the launcher directivity, is estimated to be 71% at a unit cost of \$1/W.

Several critical issues were identified during the course of this current-drive study, the most pivotal of which is the need for a full demonstration of the fast-wave current-drive technique in a tokamak plasma. Secondly, demonstration of efficient coupling of fast-wave power from the folded waveguide to a toroidal plasma is an important goal for future experiments. Finally, RF tubes with $\sim$90% efficiency and $\sim$5-MW continuous-wave (CW) output power need to be developed.

REFERENCES

[1] D. A. Ehst, Y. Cha, A. M. Hassanein, *et al.*, "Tokamak Burn Cycle Study: A Data Base for Comparing Long Pulse and Steady-State Power Reactors—Part I," *Nucl. Eng. Des./Fusion* **2** (1985) 305.

[2] D. A. Ehst, Y. Cha, A. M. Hassanein, *et al.*, "Tokamak Burn Cycle Study: A Data Base for Comparing Long Pulse and Steady-State Power Reactors—Part II," *Nucl. Eng. Des./Fusion* **2** (1985) 319.

[3] C. C. Baker, M. A. Abdou, R. M. Arons, A. E. Bolon, C. D. Boley, J. N. Brooks, *et al.*, "STARFIRE—A Commercial Tokamak Fusion Power Plant Study," Argonne National Laboratory report ANL/FPP-80-1 (1980).

[4] N. J. Fisch, "Theory of Current Drive in Plasmas," *Rev. Mod. Phys.* **59** (1987) 175.

[5] R. J. Bickerton, J. W. Connor, and J. B. Taylor, "Diffusion Driven Plasma Currents and Bootstrap Tokamak," *Nature Phys. Sci.* **229** (1971) 110.

[6] M. C. Zarnstorff, M. G. Bell, M. Bitter, *et al.*, "Bootstrap Current in TFTR," *Phys. Rev. Lett.* **60** (1988) 1306.

[7] J. G. Cordey, C. D. Challis, and P. M. Stubberfield, "Bootstrap Current Theory and Experimental Evidence," *Plasma Phys. and Controlled Fusion* **30** (1988) 1625.

[8] M. Kikuchi, M. Azumi, S. Tsuji, *et al.*, "Bootstrap Current During Perpendicular Neutral Injection in JT-60," *Nucl. Fusion* **30** (1990) 343.

[9] M. K. Bevir, C. G. Gimblett, and G. Miller, "Quasi-Steady-State Toroidal Discharge," *Phys. Fluids* **28** (1985) 1826.

[10] T. H. Stix and M. Ono, "Viscous Current Drive," Princeton Plasma Physics Laboratory report PPPL-2211 (1985).

[11] C. W. Hartman, W. L. Barr, J. L. Eddleman, *et al.*, "Acceleration of Compact Toroid Plasma Rings for Fusion Applications," *Proc. 12th Int. Conf. on Plasma Phys. and Controlled Nucl. Fusion Research,* Nice, France (Oct. 1988), International Atomic Energy Agency, Vienna (1989) 547.

[12] T. H. Jenzen and M. S. Chu, "Current Drive and Helicity Injection," *Phys. Fluids* **27** (1984) 2881.

[13] V. S. Chan, R. L. Miller, and T. Ohkawa, "Current Drive by Wave Helicity Injection," *Phys. Fluids B* **2** (1990) 1441.

[14] K. Ushigusa, T. Imai, Y. Ikeda, *et al.*, "Lower Hybrid Experiments in JT-60," *Proc. 12th Int. Conf. on Plasma Phys. and Controlled Nucl. Fusion Research,* Nice, France (Oct. 1988), International Atomic Energy Agency, Vienna (1989) 621.

[15] S. Itoh, N. Hiraki, Y. Nakamura, *et al.*, "Steady State Current Drive by Lower Hybrid Wave in TRIAM-1M Tokamak," *Proc. 12th Int. Conf. on Plasma Phys. and Controlled Nucl. Fusion Research,* Nice, France (Oct. 1988), International Atomic Energy Agency, Vienna (1989) 629.

[16] T. C. Simonen, M. Matsuoka, D. K. Bhadra, *et al.*, "Neutral-Beam Current-Driven High-Poloidal-Beta Operation of the DIII-D Tokamak," *Phys. Rev. Lett.* **61** (1988) 1720.

[17] T. Yamamoto, H. Aikawa, K. Hoshino, *et al.*, "Improvement of RF Current Drive Density Limit in the JFT-2M Tokamak," *Proc. 12th Int. Conf. on Plasma Phys. and Controlled Nucl. Fusion Research,* Nice, France (Oct. 1988), International Atomic Energy Agency, Vienna (1989) 733.

[18] M. Ono, G. J. Green, D. Darrow, *et al.*, "Steady-State Tokamak Discharge via DC Helicity Injection," *Phys. Rev. Lett.* **59** (1987) 2165.

[19] M. J. Schaffer, S. Yamaguchi, "AC Helicity Injection Current Drive Experiments in DIII-D," in *U.S.-Japan Workshop on Advanced Current Drive Concepts*, Lawrence Livermore National Laboratory report MISC-4551 (1988).

[20] D. S. Darrow, M. Ono, C. B. Forest, *et al.*, "Properties of DC Helicity Injected Tokamak Plasmas," *Phys. Fluids B* **2** (1990) 1415.

[21] B. I. Cohen, R. H. Cohen, G. D. Kerbel, *et al.*, "Microwave Heating and Current Drive in Tokamaks," *Proc. 12th Int. Conf. on Plasma Phys. and Controlled Nucl. Fusion Research,* Nice, France (Oct. 1988), International Atomic Energy Agency, Vienna (1989) 759.

[22] R. H. Cohen, P. T. Bonoli, M. Porkolab, *et al.*, "Pulsed Lower-Hybrid Wave Penetration in Reactor Plasmas," *Proc. 8th Top. Conf. on Appl. of Radio-Frequency Power to Plasmas,* Irvine, CA (1989) *AIP Conf. Proc.* **190** (1989) 126.

[23] T. Imai, H. Kimura, Y. Kusame, *et al.*, "Lower Hybrid Current Drive and Higher Harmonic ICRF Heating Experiments on JT-60," in *Proc. 13th Int. Conf. on Plasma Phys. and Controlled Nucl. Fusion Research,* Washington, D.C. (Oct. 1990), International Atomic Energy Agency, Vienna (1991).

[24] F. C. Jobes, S. Bernabei, T. K. Chu, *et al.*, "Start-Up and Ramp-Up of the PLT Tokamak by Lower Hybrid Waves," *Phys. Rev. Lett.* **55** (1985) 1295.

[25] T. K. Mau, "Role of Alpha Particle Damping in Fast Wave Current Drive and Heating," *Proc. 8th Top. Conf. on Appl. of Radio-Frequency Power to Plasmas,* Irvine, CA (1989) *AIP Conf. Proc.* **190** (1989) 158.

[26] F. L. Hinton and R. D. Hazeltine, "Theory of Plasma Transport in Toroidal Confinement Systems," *Rev. Mod. Phys.* **48** (1976) 239.

[27] D. A. Ehst, "Toroidal Equilibrium with Low Frequency Wave Driven Currents," *Nucl. Fusion* **25** (1985) 629.

[28] M.-Y. Hsiao, D. A. Ehst, and K. Evans, Jr., "Bootstrap Currents in Radio-Frequency-Driven Tokamak Equilibria," *Nucl. Fusion* **29** (1989) 49.

[29] J. T. Hogan, "Neoclassical Currents Effects in Neutral-Beam-Heated Tokamak Discharges," *Nucl. Fusion* **21** (1981) 365.

[30] M. C. Zarnstorff and S. C. Prager, "Experimental Study of Neoclassical Currents," *Phys. Fluids* **29** (1986) 298.

[31] G. Becker, "Effects of Bootstrap and Beam Driven Currents on Current Profile and Ballooning Stability in ASDEX L- and H-Mode Plasmas," *Nucl. Fusion* **29** (1989) 1291.

[32] S. P. Hirshman, "Finite-Aspect-Ratio Effects on the Bootstrap Current in Tokamaks," *Phys. Fluids* **31** (1988) 3150.

[33] D. A. Ehst, "Fast Wave Current Drive: Experimental Status and Reactor Prospects," Argonne National Laboratory report ANL/FPP/TM-219 (1988).

[34] R. McWilliams, D. F. Sheehan, N. S. Wolf, *et al.*, "Fast Wave Current Drive Above the Slow Wave Density Limit," *Proc. 8th Top. Conf. on Appl. of Radio-Frequency Power to Plasmas,* Irvine, CA (1989) *AIP Conf. Proc.* **190** (1989) 126.

[35] L.-G. Eriksson and T. Hellsten, "Electron Heating During Ion Cyclotron Resonance Heating in JET," *Nucl. Fusion* **29** (1989) 875.

[36] T. Yamamoto, Y. Uesugi, H. Kawashima, *et al.*, "Observation of Direct Electron Heating by the Fast Waves in the Lower-Hybrid Range of Frequencies in the JFT-2M Tokamak," *Phys. Rev. Lett.* **63** (1989) 1148.

[37] G. Giruzzi, "Impact of Electron Trapping on RF Current Drive in Tokamaks," *Nucl. Fusion* **27** (1987) 1934.

[38] C. F. F. Karney, N. J. Fisch, and A. H. Reiman, "Green's Function for RF-Driven Current in a Toroidal Plasma," *Proc. 8th Top. Conf. on Appl. of Radio-Frequency Power to Plasmas,* Irvine, CA (1989) *AIP Conf. Proc.* **190** (1989) 430.

[39] J. G. Cordey, T. Edlington, and D. F. H. Start, "A Theory of Currents Induced by Radio-Frequency Waves in Toroidal Plasmas," *Plasma Phys.* **24** (1982) 73.

[40] S. C. Chiu, V. S. Chan, R. W. Harvey, *et al.*, "Theory of Fast Wave Current Drive in Tokamak Plasmas," *Nucl. Fusion* **29** (1989) 2175.

[41] N. J. Fisch and C. F. F. Karney, "Current Generation with Low-Frequency Waves," *Phys. Fluids* **24** (1981) 27.

[42] K. Yoshioka and T. M. Antonsen, "Neoclassical Effects on RF Current Drive in Tokamaks," *Nucl. Fusion* **26** (1986) 839.

[43] C. F. F. Karney and N. J. Fisch, "Efficiency of Current Drive by Fast Waves," *Phys. Fluids* **28** (1985) 116.

[44] N. J. Fisch and A. H. Boozer, "Creating an Asymmetric Plasma Resistivity with Waves," *Phys. Rev. Lett.* **45** (1980) 720.

[45] T. L. Owens, "A Folded Waveguide Coupler for Plasma Heating in the Ion Cyclotron Range of Frequencies," *IEEE Trans. Plasma Sci.* **PS-14** (1986) 934.

[46] A. C. England, O. C. Eldridge, S. F. Knowlton, *et al.*, "Power Transmission and Coupling for Radiofrequency Heating of Plasmas," *Nucl. Fusion* **29** (1989) 1527.

[47] T. L. Owens and G. L. Chen, "A Folded Waveguide Coupler for Ion Cyclotron Heating," *Fusion Technol.* **10** (1986) 1024.

[48] T. L. Owens, G. L. Chen, G. R. Haste, *et al.*, "Tests of a High-Power Folded Waveguide Coupler for ICRF Heating," *Proc. 7th Top. Conf. on Appl. of Radio-Frequency Power to Plasmas,* Kissimmee, FL (1987) *AIP Conf. Proc.* **159** (1987) 298.

[49] G. R. Haste and D. J. Hoffman, "High-Power Testing of the Folded Waveguide," *Proc. 7th Top. Conf. on Appl. of Radio-Frequency Power to Plasmas,* Kissimmee, FL (1987) *AIP Conf. Proc.* **159** (1987) 266.

[50] G. R. Haste, P. L. Nguyen, D. J. Hoffman, *et al.*, "Folded Waveguide Development," *Bull. Am. Phys. Soc.* **34** (1989) 2093.

[51] G. R. Haste, Oak Ridge National Laboratory, private communication (1989).

[52] S. Sharafat, University of California Los Angeles, private communication (1989).

[53] J. J. Yugo, Oak Ridge National Laboratory, private communication (1989).

[54] N. Marcuvitz, *Waveguide Handbook,* McGraw-Hill, New York (1951).

[55] "Appendix: Numerical Data," *Proc. Int. Conf. on Silicon Carbide*, University Park, PA (Oct. 1968), *Silicon Carbide—1968*, H. K. Henisch and R. Roy, Eds., Pergamon, New York (1970) p. S365.

[56] S. Ramo, J. R. Whinnery, and T. van Duzer, *Fields and Waves in Communication Electronics,* Wiley, New York (1965).

[57] Y. Takeda, K. Nakamura, K. Maeda, *et al.*, "Effects of Elemental Additives on Electrical Resistivity of Silicon Carbide Ceramics," *J. Am. Ceram. Soc.* **70** (1987) C-266.

[58] R. J. Meakins, "Mechanisms of Dielectric Absorption in Solids," *Progress in Dielectrics*, J. B. Birks and J. Hart, Eds., Wiley, New York (1961) Vol. 2, p. 151.

[59] A. R. von Hippel, *Dielectrics and Waves,* Wiley, New York (1954).

[60] S. N. Buckley, P. Agnew, "Radiation-Induced Changes in the Dielectric Properties of Insulating Ceramics at ICRH Frequencies," *J. Nucl. Mater.* **155-157** (1988) 361.

[61] W. D. Kirkpatrick, "A Criterion for Vacuum Sparking Designed to Include Both RF and DC," Lawrence Livermore National Laboratory report UCRL-2321 (1983).

[62] F. W. Perkins, R. F. Kluge, "A Resonant-Cavity ICRF Coupler for Large Tokamaks," *IEEE Trans. Plasma Sci.* **PS-12** (1984) 161.

[63] T. K. Mau, S. C. Chiu, and D. R. Baker, "Coupling Analysis for the ICRF Resonant Cavity Launcher on DIII-D," *IEEE Trans. Plasma Sci.* **PS-15** (1987) 273.

[64] M. Loring, D. Remsen, T. Fujii, *et al.*, "First Tests of the Varian Eimac X2242 at 110 and 130 MHz in the JT-60 ICRH System," *Proc. IEEE 13th Symp. on Fusion Eng.,* Knoxville, TN (Oct. 1989), IEEE No. 89CH2820-9, IEEE, Piscataway, NJ (1990) p. 1428.

[65] A. V. Haeff, "An UHF Power Amplifier on Novel Design," *Electronics* (Feb. 1939) 30.

[66] R. R. L. Staff, W. G. Dow, and H. W. Welch, *VHF Techniques,* McGraw-Hill, New York (1947) Vol. 1, p. 445.

[67] D. H. Preist and M. B. Shrader, "The Klystrode—An Unusual Transmitting Tube with Potential for UHF-TV," *Proc. IEEE* **70** (1982) 1318.

[68] M. Loring, Varian Associates, private communication (1990).

[69] P. U. Lamalle, A. M. Messiaen, and P. E. Vandenplas, "ICRH Antenna Array Analysis and Resulting Problem of Generator Matching," *IEEE Trans. Plasma Sci.* **PS-15** (1987) 60.

[70] G. G. Lister, D. E. Post, and R. Goldston, "Computer Simulation of Neutral Beam Injection into Tokamaks Using Monte Carlo Techniques," *Proc. 3th Symp. on Plasma Heating in Toroidal Devices,* Varenna, Italy (1976) 303.

[71] R. H. Fowler, J. A. Holmes, and J. A. Rome, "NFREYA—A Monte Carlo Beam Deposition Code for Noncircular Tokamak Plasmas," Oak Ridge National Laboratory report ORNL/TM-6845 (1979)

[72] D. J. Strickler, J. B. Miller, K. E. Rothe, and Y-K. M. Peng, "Equilibrium Modeling of the TFCX Poloidal Field Coil System," Oak Ridge National Laboratory report ORNL/FEDC-83/10 (1984).

[73] C. D. Boley, Lawrence Livermore National Laboratory, private communication (1989).

[74] R. K. Janev, C. D. Boley, and D. E. Post, "Penetration of Energetic Neutral Beams into Fusion Plasmas," *Nucl. Fusion* **29** (1989) 2125.

[75] J. D. Gaffey, "Energetic Ion Distribution Resulting from Neutral Beam Injection in Tokamaks," *J. Plasma Phys.* **16** (1976) 149.

[76] D. F. H. Start and J. G. Cordey, "Beam-Induced Currents in Toroidal Plasmas of Arbitrary Aspect Ratio," *Phys. Fluids* **23** (1980) 1477.

[77] D. R. Mikkelsen and C. E. Singer, "Optimization of Steady-State Beam-Driven Tokamak Reactors," *Nuclear Technol./Fusion* **4** (1983) 237.

[78] W. L. Stirling, W. R. Becraft, J. H. Whealton, *et al.*, "A Neutral Particle Beam System for ITER Employing RF Acceleration," *Proc. IEEE 13th Symp. on Fusion Eng.,* Knoxville, TN (Oct. 1989) IEEE No. 89CH2820-9, IEEE, Piscataway, NJ (1990) p. 1448.

[79] W. R. Becraft, J. H. Whealton, T. P. Wangler, *et al.*, "RF Accelerated High Energy (1–3 MeV) Neutral Beams for Tokamak Plasma Heating, Current Drive and Alpha Diagnostics," *Proc. of ANS 8th Top. Mtg. Technol. of Fusion Energy,* Salt Lake City, UT (Oct. 1988) *Fusion Technol.* **15** (1989) 734.

[80] K. Barrass, S. Cohen, F. Engelman, *et al.*, " Summary Report for the June–October Joint Work Session," Garching, Germany, ITER report ITER-IL-Ph-5-9-81 (1989).

[81] S. D. Scott, "Projections of Rotation Velocity for ITER," presented at ITER meeting on energy confinement, Garching, Germany (1988).

[82] W. M. Stacey and J. Mandrekas, "An Extension of the Theory for Neutral Beam Driven Currents in Tokamaks," Georgia Institute of Technology report GTFR-83 (1988)

[83] W. S. Cooper, "Summary of the Status of Negative-Ion Based Neutral Beams," *Nucl. Technol./Fusion* **4** (1983) 632.